The Dissertation Committee for Sung Woo Bae certifies that this is the approved version of the following dissertation:

Sustainable Microgrid and Electric Vehicle Charging Demand for a Smarter Grid

Committee:

Alexis Kwasinski, Supervisor

Aristotle Arapostathis

Mircea D. Driga

W. Mack Grady

Robert E. Hebner

Sustainable Microgrid and Electric Vehicle Charging Demand for a Smarter Grid

by

Sung Woo Bae, B.S.; M.S.E.

DISSERTATION

Presented to the Faculty of the Graduate School of

The University of Texas at Austin

in Partial Fulfillment

of the Requirements

for the Degree of

DOCTOR OF PHILOSOPHY

The University of Texas at Austin

December 2011

Dedication

To Youngjoo, Kate, and my parents for their love and support

Acknowledgements

First and foremost, I would like to extend my deepest gratitude to my dissertation supervisor, Professor Alexis Kwasinski. Whenever I struggled in academic difficulties, he guided me to correct solutions in step-by-step procedures. In addition, his encouragement and enthusiasm inspired me to successfully complete my doctoral degree at the University of Texas at Austin. Moreover, I value that he offered me various research opportunities including an algal oil extraction project and an electric vehicle project. These research opportunities provided me with fundamental ideas for this work.

In addition, I would like to acknowledge the other distinguished members of my dissertation committee: Professors Aristotle Arapostathis, Mircea D. Driga, and Mack Grady in the department of Electrical and Computer Engineering, and Director Robert E. Hebner at Center for Electromechanics. Their valuable advice and encouragement absolutely improved my dissertation and helped me to successfully complete this work. I also could not forget their warm attitudes whenever they guided me to correct directions.

I also would like to attribute the contributions of this work to my former and present classmates and friends, Jin Hur, Byungchul Jang, Hyeonsu Park,

Seunghoon Choung, Seunghyun Chun, Cheolhee Cho, Wonjin Cho, Heejung Park, Juyoung Jung, Jihoon Yoon, Myungchin Kim, Duehee Lee, Junseok Song, Joonhyun Kim, Youngsung Kwon, Han Kang, Joohyun Jin, Chimaobi Onwuchekwa, Vaidyanathan Krishnamurthy, Ruichen Zhao, Sheng Yang Yu, Harsha Kumar Maddur Chandrash, and Amir Toliyat. Special thanks to my good friends, Aaron Williams and Mark Flynn who helped me at Center for Electromechanics. Valuable discussions with them helped me to complete this work.

For last, I would like to extend the most important thanks to my family. Due to my parents' unlimited love, trust, and support, I was able to complete my doctoral degree. Although my precious daughter, Kate, deprived my wife and me of good-night sleep by the end of my doctoral studies, her adorable smiles gave me refreshment and energized me whenever I returned home from school. Last but not least, I left my deepest appreciation to my wife, Youngjoo. Without her support and sacrifice, none of my dissertation research could have been possible.

Sung Woo Bae

The University of Texas at Austin

September 2011

Sustainable Microgrid and Electric Vehicle Charging Demand for a Smarter Grid

Sung Woo Bae, Ph.D.

The University of Texas at Austin, 2011

Supervisor: Alexis Kwasinski

A "smarter grid" is expected to be more flexible and more reliable than traditional electric power grids. Among technologies required for the "smarter grid" deployment, this dissertation presents a sustainable microgrid and a spatial and temporal model of plug-in electric vehicle charging demand for the "smarter grid". First, this dissertation proposes the dynamic modeling technique and operational strategies for a sustainable microgrid primarily powered by wind and solar energy resources. Multiple-input dc-dc converters are used to interface the renewable energy sources to the main dc bus. The intended application for such a microgrid is an area in which there is interest in achieving a sustainable energy solution, such as a telecommunication site or a residential area. Wind energy variations and rapidly changing solar irradiance are considered in order to explore the effect of such environmental variations to the intended microgrid. The

proposed microgrid can be operated in an islanded mode in which it can continue to generate power during natural disasters or grid outages, thus improving disaster resiliency of the "smarter grid".

In addition, this dissertation presents the spatial and temporal model of electric vehicle charging demand for a rapid charging station located near a highway exit. Most previous studies have assumed a fixed charging location and fixed charging time during the off-peak hours for anticipating electric vehicle charging demand. Some other studies have based on limited charging scenarios at typical locations instead of a mathematical model. Therefore, from a distribution system perspective, electric vehicle charging demand is still unidentified quantity which may vary by space and time. In this context, this study proposes a mathematical model of electric vehicle charging demand for a rapid charging station. The mathematical model is based on the fluid dynamic traffic model and the M/M/s queueing theory. Firstly, the arrival rate of discharged vehicles at a charging station is predicted by the fluid dynamic model. Then, charging demand is forecasted by the M/M/s queueing theory with the arrival rate of discharged vehicles. The first letter M of M/M/s indicates that discharged vehicles arrive at a charging station with the Poisson distribution. The second letter M denotes that the time to charge each EV is exponentially distributed, and the third letter s means that there are s identical charging pumps at a charging station. This

mathematical model of charging demand may allow grid's distribution planners to anticipate charging demand at a specific charging station.

Table of Contents

List of Tables

List of Figures

Chapter 1

Introduction

1.1 SMARTER GRID

The capacity of traditional electric power grids seems to be rapidly reaching their limitations [1]. The symptoms of reaching their limitations have been shown by increased signs of stress on the electric power grids [2] such as the 2000 and 2001 California's electricity crisis [3], the 2003 blackout in the U.S. and Canada [4], and the 2003 blackout in Sweden and Denmark [4]. The fundamental problems of these crises can be traced back to the centralized architecture of the initial electric power grids in the late 1800s [2]. These centralized designs are relatively inflexible and vulnerable to natural disasters [5] or intentional attacks [2]. In order to overcome these weaknesses, the next generation electric power grids are expected to be more flexible and more resilient than the traditional electric power grids. Therefore, the next generation electric power grid is called by a “smarter grid” [1] in this dissertation. Although smart grid technologies are often considered as the advanced metering infrastructure (AMI) and real-time

pricing signals that allow electric consumers to be involved in the electric market indirectly, these AMI and real-time pricing can only provide very limited functionalities in reality [2]. Therefore, the "smarter grid" herein refers to a more advanced smart grid in which electric customers can interact with utility companies indirectly by real-time pricing signals and directly by distributed generation [6].

1.2 SCOPE OF THE WORK

Full deployment of the "smarter grid" may require incorporating various technologies to the traditional electric power grids. The most important technologies are advanced autonomous control methods, distributed energy storage, distributed generation, and plug-in electric vehicles [2]. Among these technologies, this study presents a sustainable microgrid and a spatial and temporal model of plug-in electric vehicle (EV) charging demand. This sustainable microgrid can be operated in an islanded mode in which it can continue to generate power even during natural disasters or grid outages. Thus, this sustainable microgrid can improve disaster resiliency of the power system. In addition, the spatial and temporal EV charging demand model can help to understand how the increased electrification of the consumer's transportation sector will impact on smart grids demand.

1.2.1 Sustainable Microgrid

One purpose of this study is to present the dynamic modeling technique and operational strategy of a sustainable microgrid primarily powered by wind and solar energy. These sources are integrated into the main bus through current-source-interface multiple-input dc-dc converters. In order to provide the context for the discussion, this microgrid could be applied to a telecommunication site or a residential area part of a future "smarter grid" power system. The proposed system is equipped with energy storage devices such as batteries. In addition, a utility grid connection is provided in order to replenish energy levels in case of emergency conditions such as power shortage from the renewable energy sources. Due to its diverse sources, power supply availability of such system may exceed that of the utility grid [7], [8]. Outage possibility in this power system is close to zero because it is highly unlikely that all energy sources in this power system are unavailable at the same time. Moreover, the combination of a wind generator and photovoltaic modules may reduce vulnerability to natural disasters [9]-[12] because they do not require lifelines.

1.2.2 Plug-in Electric Vehicle Charging Demand

The other goal of this study is to present the spatial and temporal model of electric vehicle (EV) charging demand for a rapid charging station on a highway.

In order to limit the scope of the analysis, this study only focuses on the charging station on a highway and not on urban or rural roads. Commercial plug-in electric vehicles (PEVs) have been produced by a few automakers such as Cooper, Nissan, and Tesla, and the first generation of plug-in hybrid electric vehicles (PHEVs) has been emerging into the market since 2010 [13]. This transportation electrification is expected to reduce gasoline consumption, thus, decreasing greenhouse gas emissions [14]-[17]. However, [18] showed that un-controlled day-time EV charging pattern may increase stress on the power system during the peak-time, which may result in extensive grid outages. On the other hand, a recent study [19] concluded that the transportation electrification can fuel up to 84 % of the U.S. light-duty vehicle fleet with the existing electricity infrastructure in the U.S. However, since the analysis in [19] is based on a "valley-filling" approach, the "infrastructure" mentioned in [19] refers to the generation infrastructure. In fact, [19] also acknowledged that additional limitations may exist in distribution transformers. These limitations are aggravated by the uneven PEVs and PHEVs penetration favoring high-income areas [20], by the temporally and spatially changing nature of PEVs and PHEVs as loads [21], and by distribution planning difficulties caused by lack of historic data on PHEVs and PEVs behavior as loads. Reference [19] also acknowledged that high PEVs and PHEVs penetration may lead to higher electricity costs, lower reliability, and effects that could even

worsen the impact of extreme events or grid emergencies to society. Thus, although PHEVs and PEVs are identified as one of smart grid motivating technologies [1], their highly disruptive impact if left unaddressed may hinder both smart grid development and PHEV adoption. Thus, it is critically important to understand how the increased electrification of the consumer's transportation sector will impact on smart grids demand in order to avoid PHEVs and PEVs to become smart grid's "killer app" [1].

1.3 Problem Descriptions, Methodology, and Contributions

1.3.1 Problem Descriptions

1.3.1.1 Sustainable Microgrid

Among the earlier work in the literature, the idea of developing a sustainable microgrid for telecommunication applications using multiple-input dc-dc converters was introduced in [11] and expanded in [22]. A variant of such system with a different multiple-input converter topology was later on described in [23] suggested a telecommunication power system in which a diesel generator and an automatic transfer switch were replaced with fuel cells and a micro-turbine using a multiple-input dc-dc converter. The power system in [11] and [22] had the following advantages: (1) the use of the multiple-input dc-dc converter reduces

unnecessary redundancy of additional parallel converters in each energy source, and (2) the investment in micro-sources is recuperated because the energy sources in this power system can be used during normal operation as well as grid power outages [10], [11], [22], [23]. Nevertheless, one issue with the system in [23] is that it still requires fuel for the local sources in normal operation.

In addition, the daily complementary generation profiles of a wind turbine and a photovoltaic module [24], [25] have stimulated research on similar power systems with a dc link method rather than an ac coupling method [26]-[37]. However, these similar power systems in [26]-[37] combined renewable energy sources with parallel dc-dc converters which may lead to unnecessary redundancy in components of the power systems. This problem can be resolved with an alternative combining method which uses multiple-input dc-dc converters previously proposed in [7], [8], [11], [22]-[23], [38]-[52]. In addition to removing redundant converters, a multiple-input dc-dc converter had other advantages such as the possibility of de-centralized control and modularity. Despite these promising advantages, few studies seem to have explored the dynamic modeling technique for the wind/solar hybrid power system with multiple-input dc-dc converters in contrast to those parallel converters. Although the hybrid power systems in [45] and [47] considered a wind generator as a local source for a multiple-input converter, they did not consider the dynamics of wind energy and

the ac characteristics of a wind generator which likely affect the controllability and performance of the system.

1.3.1.2 Plug-in Electric Vehicle Charging Demand

Despite the recognized importance of developing spatial and temporal electric vehicle (EV) charging demand, almost none of the studies seem to have explored the charging demand at a rapid charging station although it can severely increase electricity demand during the peak-time. Most of previous studies [17], [19], [53]-[58] have postulated a fixed charging location—e.g. in a residential area—and fixed charging starting time, most of which occurs in the evening or at night.

Although some studies [18], [59]-[63] on EV charging demand have been based on limited charging scenarios and deterministic models, these studies may not be able to capture the uncertainties of EV users' charging behaviors. EV charging demand was predicted in [59] and [60] with three charging scenarios based on electricity tariff structures (i.e., fixed, time-of-use, and real-time electricity rate). These electricity tariffs were considered to determine EV charging behaviors in the uncontrolled, controlled off-peak, and smart charging scenarios respectively. In the controlled off-peak charging scenario, economic incentives are provided to EV users in order to shift the load curve. In the smart

charging scenario, EV users are expected to charge their EVs with a real-time electricity rate. Reference [61] investigated EV charging demand in the distribution system in Stockholm, Sweden based on a six-step scenario planning method [64]. This study [61] also considered two charging behaviors called by unregulated and regulated charging. In the case of unregulated charging, EV users charge their vehicles on their interests since they don't receive any incentives for charging and information on the electricity rate. EV users in the regulated charging case receive the incentive that is designed to fill the "valleys" in the load curve [19]. The authors in [62] also studied EV charging load profiles with similar charging scenarios (i.e., dumb charging and dual tariff policy corresponding to uncontrolled and controlled off-peak charging respectively). However, in the smart charging they focused more on utility companies' interests such as congestion prevention and voltage control. In this smart charging, utility companies can actively control EV charging demand by a hierarchical management system. Although some studies [18], [63] used the Bass model [65] in order to predict the penetration of EVs, these studies still used uncontrolled and controlled charging scenarios.

In contrast, several researchers [21], [66]-[69] have proposed methods for anticipating EV charging demand with stochastic models; however, these studies are still limited to EV charging demand in residential areas. An EV user may want

to charge his/her vehicle at a rapid charging station when he/she forgets to charge it at night. This behavior is similar to that of a conventional gasoline vehicle user who can refuel the vehicle at any gas stations and any time. Reference [68] attempted to predict domestic EV charging demand in the UK by a sequential Monte Carlo method with historical driving data on thousands of conventional vehicle users from the UK Time of Use Survey 2000 [70]. Although [68] may estimate stochastic EV charging demand, its analysis is still limited because charging behaviors were assumed to be unregulated since there were no incentives or smart charging methods and it only focused on EV charging demand in residential areas. On the other hand, [21], [66], [67] considered smart charging schemes when they predicted EV impacts on residential distribution networks with probabilistic analyses. Reference [69] anticipated EV charging demand in residential areas with the $M/M/n_{max}$ queueing theory; however, its analysis may not be reliable since the mean inter-arrival time to a charging location is assumed to equal the mean charging completion time.

Some other precedent studies [71]-[73] have suggested EV charging demand at various locations such as residential areas, office areas, retail areas, and public parking lots. Specifically, [71] anticipated EV charging demand in these areas through a survey from potential EV users. However, these studies

[71]-[73] used limited charging scenarios at typical locations instead of a mathematical model of EV charging demand.

1.3.2 Methodology and Contributions

1.3.2.1 Sustainable Microgrid

This study presents the dynamic modeling and control strategy of a wind/ solar hybrid power system with a multiple-input dc-dc converter in which the dynamics of wind energy and the ac modeling are considered in the wind generator model. A direct-driven permanent magnet synchronous generator (PMSG) is used for the wind generator model because a direct-driven PMSG has drawn attention for the residential-scale power level due to its gearless system which does not require frequent mechanical maintenance. Moreover, PMSG's control hardware is simpler than brushed machine's hardware since it does not require a dc excitation circuit because of its permanent magnet excitation [74]. In addition to the dynamics of wind energy, this study also considers the rapidly changing solar irradiance that may happen during the day and that affects generated power from photovoltaic modules in the proposed power system. Moreover, the herein proposed microgrid does not require any fuel for the local sources because it is powered by inherently self sustainable energy sources. Thus, it does not rely on lifelines—e.g., roads or pipes for fuel or natural gas delivery—

for operation, which makes it a truly self sustainable power system ideal to provide power not only in normal conditions but also during extreme events when lifeline operation is not expected. Furthermore, the proposed power system not only can produce electricity from the renewable energy sources but may also inject surplus power to the utility grid in normal operation.

1.3.2.2 Plug-in Electric Vehicle Charging Demand

This study also presents the mathematical model of rapid charging station's electricity demand which may vary both spatially and temporally. Specifically, the methodology of this mathematical model is based on the fluid traffic model [75]-[77] and the M/M/s queueing theory [78]. Firstly, the arrival rate of discharged electric vehicles at a specific charging station is anticipated by the fluid traffic model proposed in wireless communication studies [75]-[77]. The idea of this fluid traffic model was introduced as the highway Poisson-Arrival-Location Model (PALM) in [77] and expanded in [75] and [76]. This traffic model was called by the highway PALM since these studies assumed that vehicles enter a highway with the Poisson distribution. The purpose of the highway PALM was to study the performance of wireless communication network on a highway such as calling and hand-off rates of mobiles [75]-[77]. Although the mobile user can initiate a call at any location on a highway, an EV user may only charge the

vehicle at a specific location, generally a charging station near a highway exit. Therefore, the fluid traffic model here is modified from the highway PALM in [75]-[77]. Secondly, EV charging demand is predicted by the M/M/s queueing theory [78] once the arrival rate of discharged electric vehicles at a specific charging station is identified. The first letter M of M/M/s indicates that discharged vehicles arrive at a charging station with the Poisson distribution. The second letter M denotes that the time to charge each EV is exponentially distributed, and the third letter s means that there are s identical charging pumps at a charging station. Details of the M/M/s queueing theory [78] will be described in Section 4.3.2.

This mathematical model of charging demand may allow grid's distribution planners to anticipate a charging demand profile for a specific charging station. The charging demand profile may also facilitate determination of the size of energy storage systems in the charging station in order to charge EVs during the peak-time by the extra energy saved from the off-peak time. With this load shifting strategy, the charging station may participate in a demand response program [79]-[83] since the charging demand at the rapid charging station is expected to sharply increase during the day, although contrary to conventional demand response techniques, the charging station participation is based on actual, not virtual, energy storage. Energy storage systems at a charging

station may also allow EVs to be charged by a diverse combination of energy sources, such as renewable energy sources in addition to the utility grid. Moreover, the mathematical model of charging demand requires relatively known traffic data such as traffic velocities which can be accessed through Global Positioning Systems (GPSs) or Closed-Circuit Televisions (CCTVs) on a highway without much difficulty [84]-[87].

1.4 ORGANIZATION OF THE DISSERTATION

The remainder of this dissertation is organized as follows. Chapter 2 describes the dynamic modeling technique of a sustainable microgrid primarily powered by wind and solar energy resources. In this chapter, the architecture and integrated components of the proposed sustainable microgrid are discussed for a dynamic modeling purpose.

Chapter 3 presents control strategies of the sustainable microgrid presented in Chapter 2. In this chapter, the simulated results and discussion of the proposed microgrid are described in order to illustrate the dynamics of the proposed power system.

Chapter 4 presents the spatial and temporal model of electric vehicle charging demand for a rapid charging station located near a highway exit. First, the detailed highway model in this study is described. Second, the model

formulations of a deterministic fluid model and a stochastic model are discussed. Then, a numerical example is presented in order to illustrate spatial and temporal dynamics captured by the proposed charging demand model for a rapid charging station.

Chapter 5 presents flexible charging strategies for a rapid charging station on a highway. A sustainable microgrid which may enable these flexible charging strategies for the rapid charging station is also presented in this Chapter.

Chapter 6 summarizes and concludes this dissertation. Finally, it is followed by the list of references.

Chapter 2

Dynamic Modeling of a Sustainable Microgrid with Wind and Solar Energy Resources

2.1 INTRODUCTION

This chapter presents a dynamic modeling for a sustainable microgrid primarily powered by wind and solar energy resources. Multiple-input dc-dc converters are used to interface the renewable energy sources to the main dc bus. The intended application for such a microgrid is an area in which there is interest in achieving a sustainable energy solution, such as a telecommunication site or a residential area part of a future smarter grid. Wind energy variations and rapidly changing solar irradiance are considered in this study in order to explore the effect of such environmental variations to the intended microgrid. A direct-driven permanent magnet synchronous wind generator is used because it has drawn attention for the residential-scale power level due to low maintenance

requirements and simple control hardware. The proposed power system not only can produce electricity from the renewable energy sources but may also inject surplus power to the utility grid.

The rest of this chapter is organized as follows. The architecture and integrated components of the proposed microgrid for a dynamic modeling purpose are discussed in Sections 2.2 and 2.3 respectively. Section 2.4 concludes with the summary of findings. The control strategies and simulation studies of the proposed power system will be discussed in Chapter 3.

2.2 PROPOSED SUSTAINABLE MICROGRID ARCHITECTURE

Figure 2.1 shows the architecture of the proposed microgrid with wind and photovoltaic (PV) resources. Its main energy sources, wind and solar radiation, are transformed in a wind generator and photovoltaic modules as indicated in Fig. 2.1. In order to combine these energy sources, a current-source-interface (CSI) multiple-input (MI) converter, such as an MI Ćuk converter or an MI SEPIC converter [43] with a dc bus system, is used because an MI CSI converter is more effective for maximum power point tracking in photovoltaic modules and for the input current control method used in this power plant. MI converters were chosen because they provide a cost-effective and flexible method to interface various renewable energy sources [11], [22], [43]. In addition, a dc power distribution

system is chosen because dc power systems may achieve higher availability and energy efficiency in a simpler way than equivalent ac power systems [7], [8], [88]. A voltage level of 380 V is considered to be the main dc bus voltage in this microgrid because it is more suitable for bidirectional power flow between the intended power system and the utility grid [22] and because it is the likely voltage to be chosen in a future standard for industrial applications with dc distribution, such as in data centers. The higher bus voltage system than conventional power plants also reduces both copper costs and cables installation costs because conductors have a smaller cross-sectional area [22], [89]. As depicted in Fig. 2.1, energy storage devices are also connected to the main dc bus in order to overcome the intermittent properties of renewable energy sources and to support local power production in an islanded mode particularly during blackouts or natural disasters.

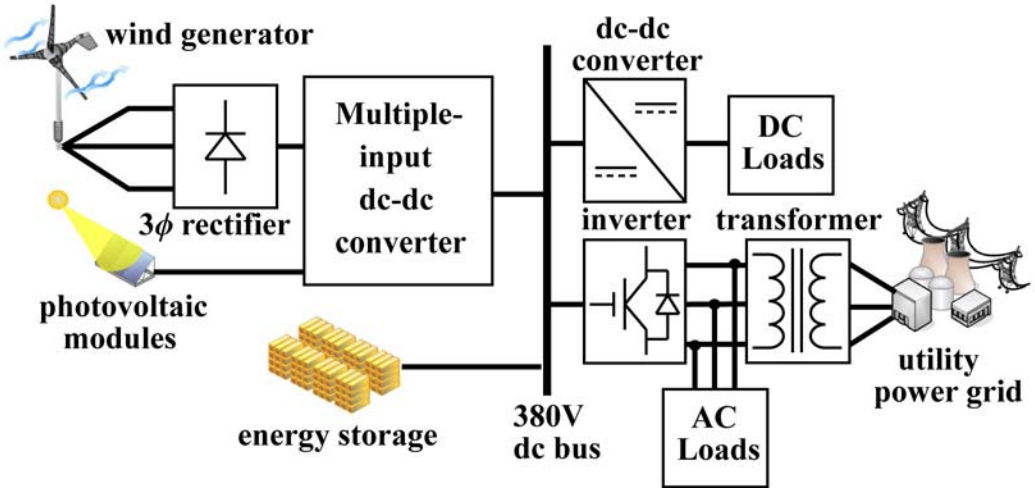

Figure 2.1: Architecture of the proposed microgrid with wind and PV resources.

As shown in Fig. 2.1, dc loads in a telecommunication application require an additional dc-dc converter in order to meet the traditional terminal voltages, such as 24 or 48 V. If the proposed system is used in a residential area part of a future "smarter grid" power system, a plug-in electric vehicle can be a dc load in such system. Ac loads can be connected to the conjunction between an inverter and a transformer, as also shown in Fig. 2.1. This conjunct configuration for the ac loads ensures that power can be always delivered from the renewable energy sources, batteries, or the utility grid.

2.3 DESCRIPTIONS OF MODELING COMPONENTS OF THE PROPOSED MICROGRID

2.3.1 Dynamic Wind Model

This study uses a wind model presented in [90] which allows us to simulate the spatial effect of dynamic wind components such as gusting, rapid ramp changes, and background noises. This dynamic wind model has four components and is defined by [90]

$$V_{wind} = V_{base} + V_{gust} + V_{ramp} + V_{noise}, \tag{2.1}$$

where V_{base} is a base wind velocity, V_{gust} is a gust wind component, V_{ramp} is a ramp wind component, and V_{noise} is a background noise wind component. The base wind component is constant, and the gust wind component can be

represented with a cosine function. The ramp wind component is used for mimicking rapid wind changes, and the noise wind component is implemented by random noises. Figure 2.2 shows this dynamic wind model used for the simulation study which will be discussed in Chapter 3.

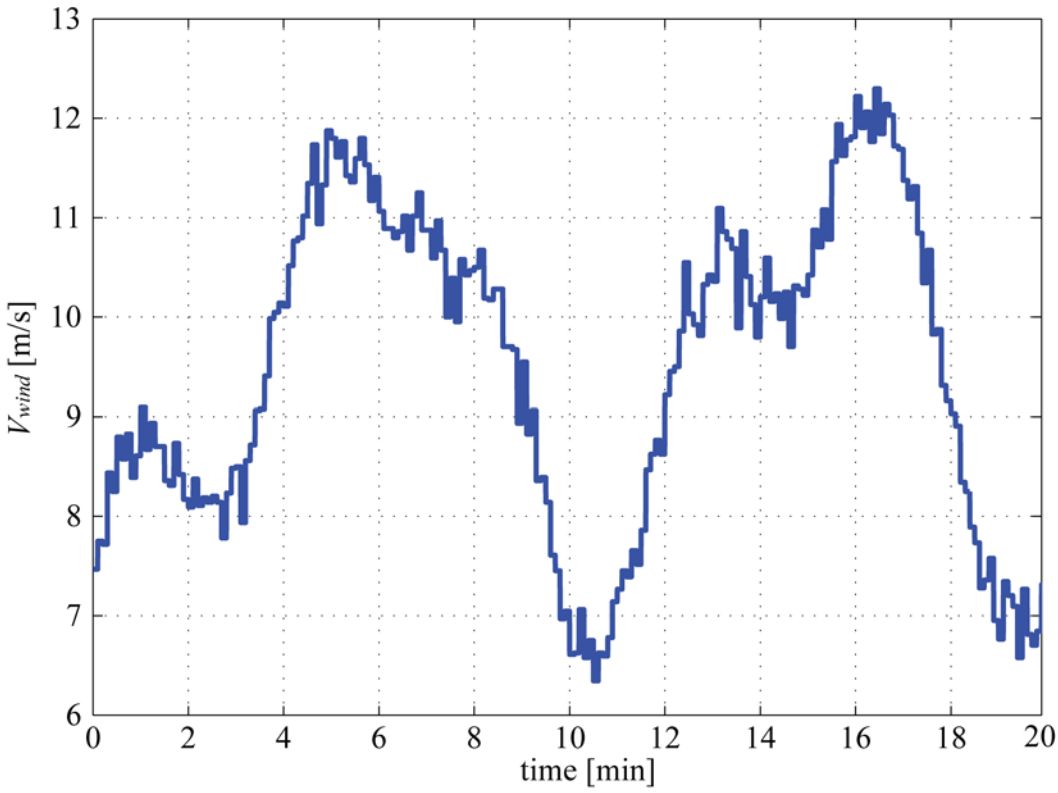

Figure 2.2: Dynamic wind model used for the simulation study.

2.3.2 Wind Turbine Model

The mechanical power (P_m) captured by the wind blades of a wind turbine is described as follows [91]:

$$P_m = \frac{1}{2} C_p(\beta, \lambda) \rho \pi R^2 V_{wind}^3 \tag{2.2}$$

where C_p is the power coefficient of a rotor, β is the pitch angle of a blade, λ is a tip-speed ratio (TSR), ρ is an air density, R is the radius of a wind turbine blade, and V_{wind} is a wind speed. A TSR can be defined as the function of a wind speed [35], [36], [91] written as

$$\lambda = \frac{\omega_m R}{V_{wind}} \tag{2.3}$$

where ω_m is the rotor speed of a wind turbine. Then, from (2.2), (2.3), and considering that $T_m = P_m/\omega_m$, the aerodynamic input torque (T_m) by which a wind generator is driven can be obtained as follows [35], [36]:

$$T_m = \frac{C_p(\beta, \lambda) \rho \pi R^5}{2\lambda^3} \omega_m^2 . \tag{2.4}$$

The rotor power coefficient (C_p) depends on the blade aerodynamics, which is the function of a blade pitch angle (β) and a tip-speed ratio (λ) [35], [36], [91]. The rotor type of a wind turbine may also be another factor affecting the rotor power coefficient (C_p). However, the C_p of [91] in which a general blade type was assumed is used in this study for the sake of simplicity [35], [36]:

$$C_p = (0.44 - 0.0167\beta)\sin\frac{\pi(\lambda - 2)}{13 - 0.3\beta} - 0.00184(\lambda - 2)\beta\,. \qquad (2.5)$$

The parameters of the investigated wind turbine model in this study are shown in Table 2.1. According to (2.4) and (2.5), the aerodynamic torque is maximized at a given wind speed when the blade pitch angle (β) is 0º. Therefore, a constant pitch angle (β = 0º) is used in this study as shown in Table 2.1.

Table 2.1: Parameters and specifications of the wind turbine model.

parameter	value	unit
rated power	20	*kW*
rated wind speed	12	*m/s*
rated rotor speed	27.5413	*rad/s*
blade radius	3.7	*m*
blade pitch angle	0	degree
air density	1.225	kg/m^3

2.3.3 Direct-driven Permanent Magnet Synchronous Generator

The wind generator considered here is a gearless direct-driven permanent magnet synchronous generator (PMSG). This PMSG does not require frequent mechanical maintenance because it does not use gears between wind blades and the generator. A low mechanical speed, one disadvantage of the gearless system, does not cause any problems because the proposed power system uses not only a power electronics interface for variable wind speed control but also a multi-pole PMSG. Another advantage of the direct-driven PMSG is that a permanent magnet

eliminates the dc excitation circuit that may complicate the control hardware [74]. Table 2.2 shows the specifications of the direct-driven PMSG model used in the simulation study.

Table 2.2: Specifications of the direct-driven permanent magnet synchronous generator model.

Parameter	value	unit
rated power	20	kW
rated line voltage	519.6	V_{rms}
stator phase inductance	8.5	mH
stator phase resistance	0.05	Ω
number of poles	12	
rated mechanical speed	263	rpm
electrical base frequency	26.3	Hz

2.3.4 Photovoltaic Module Model

Several circuit-based photovoltaic (PV) models that mimic PV arrays non-linear I-V characteristic have been proposed in the literature. Among them, the PV model proposed in [92] is used in this study because it is a circuit-based model suitable for commercial PV systems. Another advantage of the PV model in [92] is that it only requires a few parameters, such as an open-circuit voltage and a short-circuit current, which every commercial PV module includes in its datasheet. Moreover, this PV model is able to represent solar irradiance and temperature changes which may happen commonly during the day [92].

The rated power of the PV system simulated in this study is 10 kW, which is composed of fifty KC200GTs manufactured by Kyocera Solar Energy Inc. The configuration of the simulated PV system is an array of 5 by 10 modules which are arranged in a rectangular shape. Figure 2.3 shows the nominal I-V and P-V characteristics of the investigated 10 kW PV array system. As indicated in Fig. 2.3, the maximum power point of the PV system is 10 kW which is achieved for 261.3 V and 38.1 A.

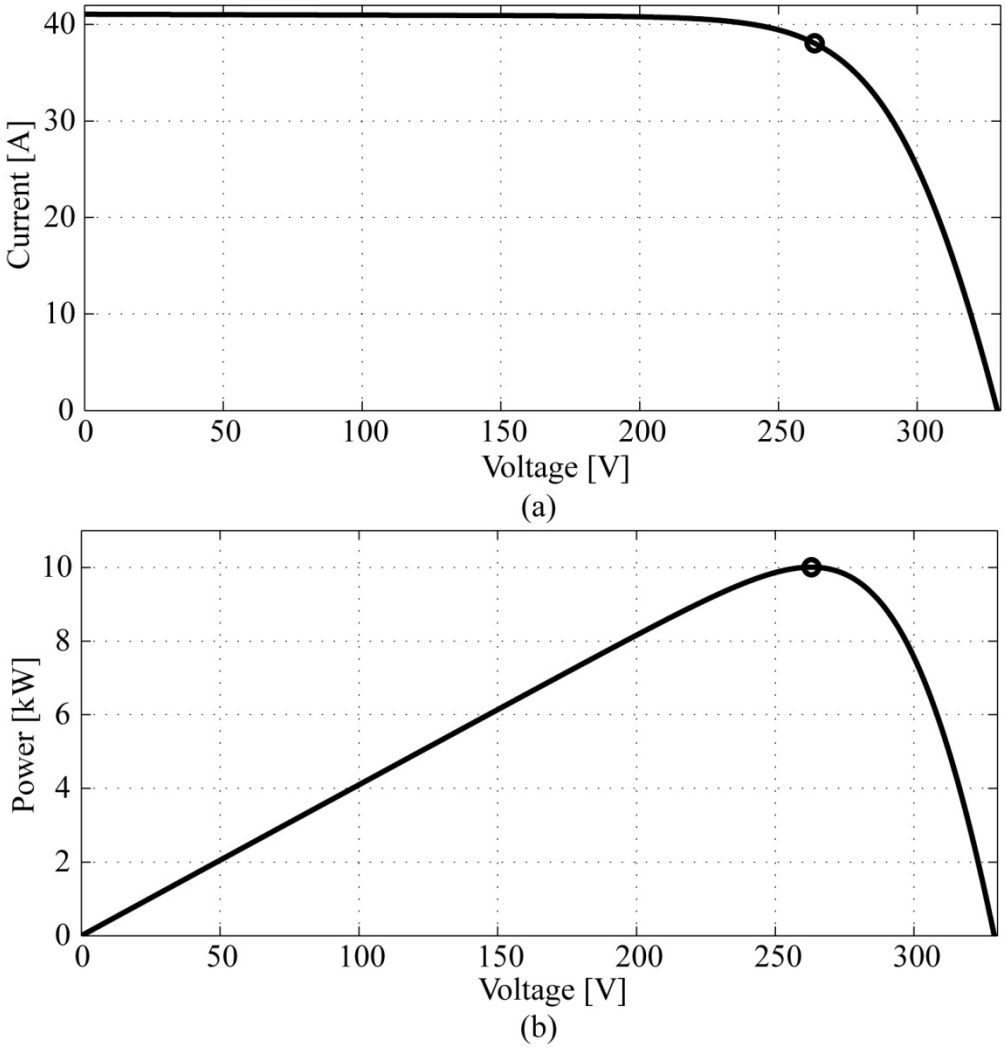

Figure 2.3: Electrical characteristics of 10 kW photovoltaic modules. (a) Current vs. voltage characteristics. (b) Power vs. voltage characteristics.

2.3.5 Multiple-input Current-source-interface Converter

Among multiple-input (MI) dc-dc converter topologies in [7], [8], [11], [22]-[23], [38]-[52], MI current-source-interface (CSI) converters such as an MI

Ćuk converter [38], [43], [52] and an MI SEPIC converter [43], [51], [52] can be used in the proposed power system because of two reasons. Firstly, these MI CSI converters are more suitable for the input current control method which will be used in this power plant and is explained in Chapter 3. Secondly, these MI CSI converters provide nearly continuous input current waveforms due to their CSI input legs. Hence, these MI CSI converters provide more operational flexibility than an MI buck-boost converter [39], [40] because these converters allow the integration of input sources that require a relatively constant current, such as a current controlled permanent magnet synchronous generator [38]. Simulated results of the MI Ćuk converter [38], [43], [52] are similar to those of the MI SEPIC converter [43], [51], [52] except for the output voltage inversion. However, since there are more past works focusing exclusively on the MI SEPIC [51], the analysis here focuses on the MI Ćuk converter shown in Fig. 2.4.

Figure 2.5 illustrates the switching diagram of a multiple-input Ćuk converter. If this MI Ćuk converter is assumed to be operated in a continuous conduction mode, circuit operation in a steady-state condition can be described based on the following three operational modes.

1) Mode 1 (see Fig. 2.6(a); $0 < t < D_1T_s$): It is assumed that the voltage level of the first input source (V_{in1}) is higher than that of the second input source (V_{in2}). Although active switches Q_1 and Q_2 are turned on in this mode as depicted in Fig.

2.5, only Q_1 conducts current since the diode Q_{d2} is reverse-biased due to the assumption that V_{in1} is greater than V_{in2}. The diode D at the common output stage is also reverse-biased.

2) Mode 2 (see Fig. 2.6(b); $D_1T_s < t < D_2T_s$): As illustrated in Fig. 2.5, only an active switch Q_2 is turned on and conducts current in this mode since the diode Q_{d2} is also turned on. The diode D at the common output stage is still reverse-biased.

3) Mode 3 (see Fig. 2.6(c); $D_2T_s < t < T_s$): All switches except the diode D are turned off in this mode. Therefore, the diode D only conducts current.

Based on the described operational modes, the switched dynamic model of this MI Ćuk converter in continuous conduction mode is governed by

$$\begin{cases} L_1 \dfrac{di_{L1}}{dt} = V_{in1} - q_{2eff}(t)(v_{c1} - v_{c2}) - (1 - q_2(t))v_{c1} \\ L_2 \dfrac{di_{L2}}{dt} = V_{in2} - q_1(t)(v_{c2} - v_{c1}) - (1 - q_2(t))v_{c2} \\ L \dfrac{di_L}{dt} = q_1(t)v_{c1} + q_{2eff}(t)v_{c2} - v_o \end{cases}, \tag{2.6}$$

$$\begin{cases} C_1 \dfrac{dv_{C1}}{dt} = (1 - q_1(t))i_{L1} - q_1(t)(i_L + i_{L2}) \\ C_2 \dfrac{dv_{C2}}{dt} = (1 - q_{2eff}(t))i_{L2} - q_{2eff}(t)(i_L + i_{L1}) \\ C \dfrac{dv_o}{dt} = i_L - \dfrac{v_o}{R} \end{cases}, \tag{2.7}$$

$$\begin{cases} q_{1eff}(t) = q_1(t) \\ q_{2eff}(t) = q_2(t) - q_1(t) \end{cases}, \tag{2.8}$$

where $q_1(t)$ and $q_2(t)$ are the switching functions of the MI Ćuk converter, and $q_{1eff}(t)$ and $q_{2eff}(t)$ are the effective switching functions of each input cell respectively. In an average sense, the derivatives of an inductor current and a capacitor voltage are zero. In addition, switching functions, $q_1(t)$, $q_2(t)$, and $q_{2eff}(t)$, can be considered as duty cycles, D_1, D_2, and D_{2eff} respectively in the average model. Then, the average model of this MI Ćuk converter is equal to be

$$\begin{bmatrix} V_{c1} \\ V_{c2} \\ V_o \end{bmatrix} = \frac{1}{1-D_2} \begin{bmatrix} (1-D_{2eff})V_{in1} + D_{2eff}V_{in2} \\ D_1V_{in1} + (1-D_1)V_{in2} \\ D_1V_{in1} + D_{2eff}V_{in2} \end{bmatrix}, \tag{2.9}$$

$$\begin{bmatrix} I_{L1} \\ I_{L2} \\ I_L \end{bmatrix} = \begin{bmatrix} D_1I_L/1-D_2 \\ D_{2eff}I_L/1-D_2 \\ P_o(1-D_2)/(D_1V_{in1} + D_{2eff}V_{in2}) \end{bmatrix}, \tag{2.10}$$

where V_{c1}, V_{c2}, and V_o are the average voltages on capacitors C_1, C_2, and C respectively, and I_{L1}, I_{L2}, and I_L are the average currents of inductors L_1, L_2, and L respectively, and P_o is the output power of the MI Ćuk converter.

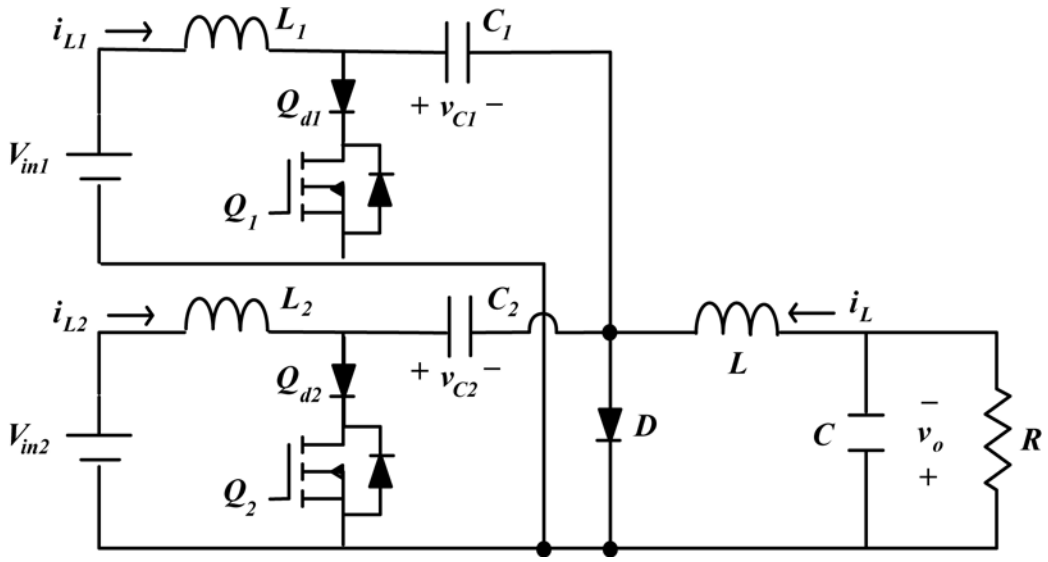

Figure 2.4: Multiple-input Ćuk dc-dc converter [38].

Therefore, the steady-state output voltage of the MI Ćuk converter is

$$V_o = \frac{D_1 V_{in1} + D_{2eff} V_{in2}}{1 - D_2}. \tag{2.11}$$

Moreover, the average output voltage in the *n*-input case can be calculated from the energy conversion rule ($\sum V_{in(i)} I_{in(i)} = V_o I_L$). The average input current for a generic leg, $I_{in(i)}$, can be obtained from the relationship that the charges delivered to each input capacitor (i.e., C_1, C_2,..., C_n) through each input inductor (i.e., L_1, L_2,..., L_n) are equal to the charge dissipated through the output stage inductor, L [93]. Thus, the average input current and output voltage in the *n*-input case are

$$I_{in(i)} = \frac{D_{eff(i)}}{1 - \sum_j D_{eff(j)}} I_L = \frac{D_{eff(i)}}{1 - \max_i (D_i)} I_L, \tag{2.12}$$

$$V_o = \frac{\sum_{i=1}^{n} D_{eff(i)} V_{in(i)}}{1 - \max_i (D_i)}, \tag{2.13}$$

where $D_{eff(i)}$ is the effective duty cycle of each input cell. If the voltage indices are arbitrarily ordered such that $V_{in1} > V_{in2} > ... > V_{in(n)}$, then

$$D_{eff(i)} = \begin{cases} 0 & ,\text{when } (D_i < \sum_{j=1}^{i-1} D_{eff(j)}) \\ D_i - \sum_{j=1}^{i-1} D_{eff(j)}, & \text{when } (D_i \geq \sum_{j=1}^{i-1} D_{eff(j)}) \end{cases}. \tag{2.14}$$

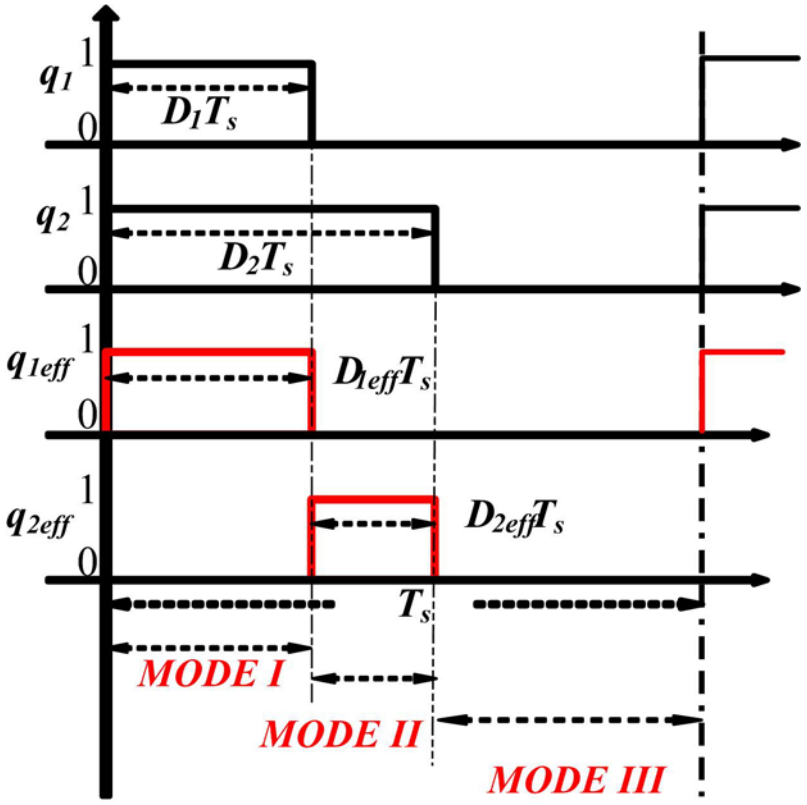

Figure 2.5: Switching diagram of the multiple-input Ćuk dc-dc converter.

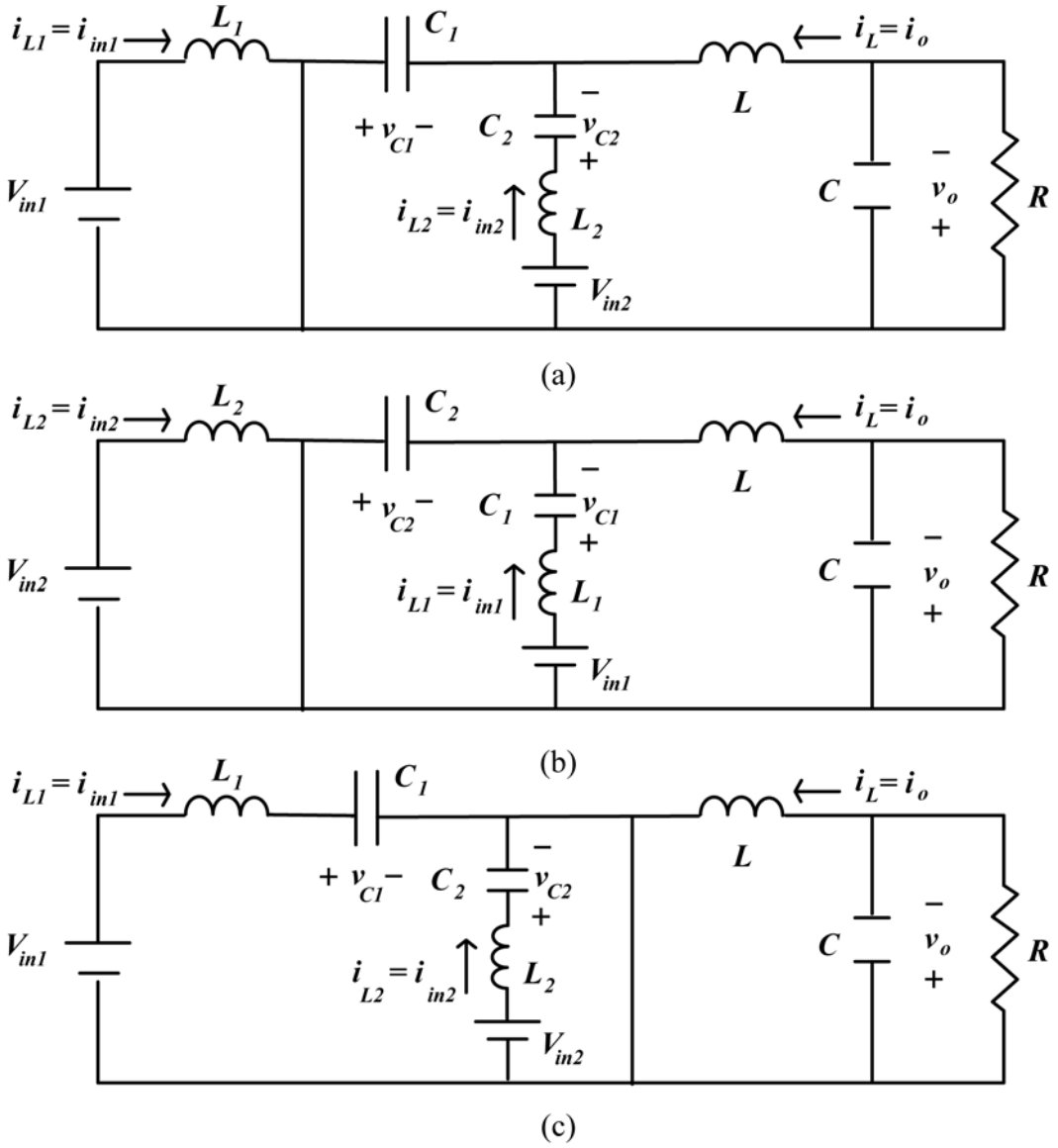

Figure 2.6: Operational modes of the multiple-input Ćuk dc-dc converter. (a) (Top) Mode I (only Q_1 conducts current). (b) (Center) Mode II (only Q_2 conducts current). (c) (Bottom) Mode III (only diode D conducts current).

2.4 CONCLUSION

This chapter presented the dynamic modeling of a sustainable microgrid primarily powered by wind and solar energy. These renewable sources are integrated into the main bus through multiple-input current-source-interface dc-dc converters. The intended application for such a microgrid is an area in which there is interest in achieving a sustainable energy solution, such as a telecommunication site or a residential area part of a future smarter grid. Wind energy variations and rapidly changing solar irradiance were considered in this study in order to explore the effect of such environmental variations to the intended microgrid. A direct-driven permanent magnet synchronous wind generator was used because it has drawn attention for the residential-scale power level due to low maintenance requirements and simple control hardware.

The proposed power system has the following advantages: (1) It is able to reduce additional parallel converters with a multiple-input dc-dc converter, (2) the dynamics of wind and solar energy and the ac modeling of the wind generator were considered in the proposed model in contrast that the previous studies in [45] and [47] with a multiple-input dc-dc converter topology did not investigate these dynamics and modeling techniques, (3) the proposed power system not only can produce electricity from the renewable energy sources but may also transmit

surplus power to the utility grid in normal operation, and (4) this power system can achieve high availability because of its diverse power supplies.

Chapter 3

Operation Strategy of a Sustainable Microgrid with Wind and Solar Energy

3.1 INTRODUCTION

This chapter presents a control method for a sustainable microgrid presented in Chapter 2. A 30 kW wind/solar hybrid power system dynamic model is developed with MATLAB Simulink/Simpowersystems. As discussed in Chapter 2, dynamic wind components (including gusting, rapid ramp changes, and noises) and rapidly changing solar irradiance are considered in the simulation study in order to explore the proposed power system's response to such environmental variations. For the wind generator, this study uses a variable speed control method whose strategy is to capture the maximum wind energy below the rated wind speed. Specifically, an input current control method is used for this variable speed control. Photovoltaic modules are controlled by an incremental conductance method in order to track their maximum power point. The simulated

dynamics of the herein proposed power system attests that the control strategy and proposed power architecture is a valid solution for a sustainable microgrid with wind and photovoltaic resources.

The rest of this chapter is organized as follows. The control strategies of the proposed power system are discussed in Section 3.2. The simulated results and discussion of the proposed microgrid are included in Section 3.3 in order to illustrate the dynamics of the proposed power system. Section 3.4 concludes with the summary of findings.

3.2 CONTROL STRATEGIES

3.2.1 Wind Turbine: Variable Speed Control

This study uses a variable speed control method whose strategy is to capture the maximum wind energy below the rated wind speed and to use a stall regulation above the rated wind speed. Figure 3.1 shows mechanical power captured by wind turbine blades at each rotor speed of the wind turbine (ω_m) and various wind speeds (V_{wind}). As Fig. 3.1 illustrates, mechanical power from the wind turbine depends on the wind turbine rotor speed (ω_m). In addition, the optimal power line can be obtained by connecting maximum power points at each wind speed because a single maximum power point exists at each wind speed as shown in Fig. 3.1. Hence, the operation of the wind turbine at the optimal rotor

speed ($\omega_{m_{opt}}$) along the optimal power curve ensures that the wind turbine captures the maximum wind energy below the rated wind speed. On the other hand, the stall regulation is used above the rated wind speed beyond which the output power of the generator is regulated at the rated power. This variable speed control strategy reduces stress in the shaft between wind blades and the wind turbine and prevents the turbine from overheating above the rated wind speed.

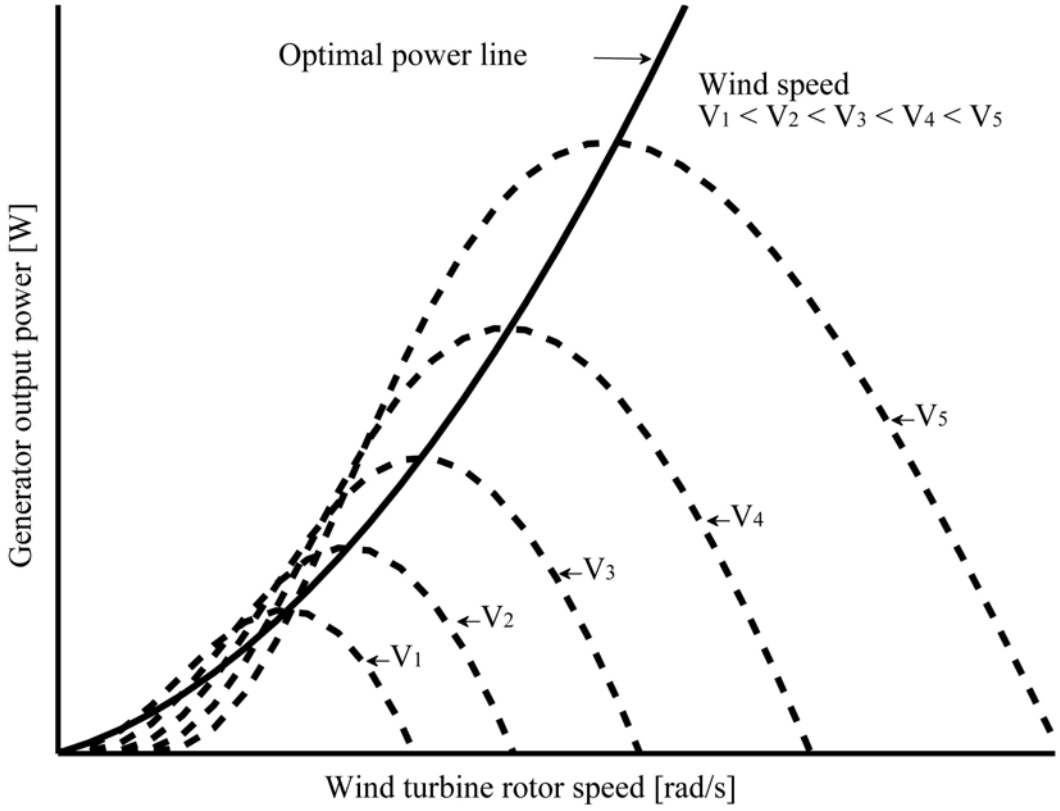

Figure 3.1: Mechanical power captured by wind turbine blades at various wind speeds [94], [95].

One feasible method to operate the wind turbine along the optimal power line below the rated wind speed is to control the output current of the three-phase rectifier (I_R) with the wind turbine rotor speed (ω_m) [35], [36], [94]-[96]. This control method requires that the wind turbine rotor speed (ω_m) is measured by a position sensor in the rotor of the wind turbine. In order to elucidate how the wind turbine can be operated on the maximum power points by controlling I_R with ω_m, the optimal mechanical power ($P_{m_{opt}}$) of the wind turbine is described as follows [94]-[96]:

$$P_{m_{opt}} = \frac{C_{p_{\max}} \rho \pi R^5}{2\lambda_{opt}^3} \omega_m^3 = K_{opt} \omega_m^3 \tag{3.1}$$

where $C_{p\max}$ is the maximum rotor power coefficient, and λ_{opt} is the optimal value of tip-speed ratios. Then, we may define an optimal power constant (K_{opt}) when a wind turbine produces the optimal mechanical power, written as [94], [95]

$$K_{opt} = \frac{C_{p_{\max}} \rho \pi R^5}{2\lambda_{opt}^3} . \tag{3.2}$$

If power efficiencies of the wind generator and the three-phase rectifier in Fig. 2.1 are assumed to be constant at η_G and η_R respectively, the real output power (P_R) from the three-phase rectifier is

$$P_R = V_R I_R = \eta_G \eta_R P_m \tag{3.3}$$

where V_R and I_R are the filtered output voltage and current from the three-phase full-bridge diode rectifier respectively. Therefore, from (3.1) and (3.3), the optimal power output at the three-phase rectifier ($P_{R_{opt}}$) can be defined as follows:

$$P_{R_{opt}} = V_R I_R = \eta_R \eta_R K_{opt} \omega_m^3 . \tag{3.4}$$

If a permanent magnet synchronous generator (PMSG) is assumed to be an ideal generator, the line-to-line voltage of a PMSG (V_{LL}) is

$$V_{LL}(t) = K_v \omega_e \sin(\omega_e t) \tag{3.5}$$

where K_v is the voltage constant of the generator, and ω_e is the electrical angular frequency of the generator. The ω_e can be expressed as the generator's mechanical speed (ω_m) and the number of poles in the generator (p) as follows:

$$\omega_e = \frac{p}{2} \omega_m . \tag{3.6}$$

Then, the dc output voltage from the three-phase rectifier (V_R) is defined as

$$V_R = \frac{3}{\pi} V_{LL_p} - \frac{3}{\pi} \omega_e L_s I_R \tag{3.7}$$

where V_{LLp} is the peak value of the line voltage which equals $K_v \omega_e$, and L_s is a stator phase inductance [97], [98]. Now, from (3.4), (3.5), and (3.7), $P_{R_{opt}}$ can be obtained as follows:

$$P_{R_{opt}} = V_R I_R = K_a \omega_m I_R - K_b \omega_m I_R^2 = \eta_G \eta_R K_{opt} \omega_m^3 . \tag{3.8}$$

where constants K_a and K_b in the third term from the left side of (3.8) are respectively defined as

$$K_a = \frac{3pK_v}{2\pi} \text{ and } K_b = \frac{3pL_s}{2\pi}. \tag{3.9}$$

By solving the quadratic equation with respect to I_R in (3.8), the reference rectified current (I_{Ropt}) is obtained by

$$I_{R_{opt}} = \frac{K_a\omega_m - \sqrt{(K_a\omega_m)^2 - 4\eta_G\eta_R K_{opt} K_b \omega_m^4}}{2K_b\omega_m}. \tag{3.10}$$

Hence, the wind turbine can be operated along the optimal power curve below the rated wind speed if I_R is controlled to its reference value (I_{Ropt}) by adjusting the duty ratios of the multiple-input dc-dc converter at each ω_m according to (3.10). On the other hand, the stall regulation is used above the rated speed beyond which I_R is regulated at the reference value (I_{Ropt}) of the rated wind speed in order to reduce mechanical stress and to prevent the wind turbine from overheating. This study uses a PI controller, depicted in Fig. 3.2, in order to achieve this target current I_{Ropt}.

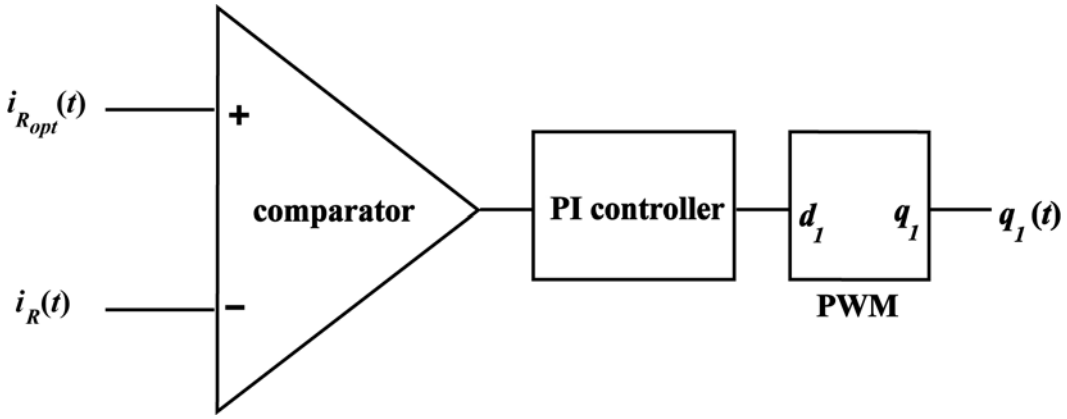

Figure 3.2: Current mode controller.

3.2.2 Photovoltaic Module: Maximum Power Point Tracking

Photovoltaic (PV) modules in the proposed microgrid are controlled so that they operate at their maximum power point (MPP). An incremental conductance method [99], [100], [101] is used for this purpose. This method uses the output current and voltage information of PV modules based on polarity changes in the derivative of PV modules' power with respect to their voltage, which is zero at the MPP, positive at the left of the MPP, and negative at the right of the MPP. The characteristics of these voltage polarity changes lead to the following criteria that identify whether PV modules reach their MPP or not [99], [100], [101]:

$$\frac{dP}{dV} = \frac{d(VI)}{dV} = I + V\frac{dI}{dV} = 0 \quad \text{(at the MPP)}, \tag{3.11}$$

$$I + V\frac{dI}{dV} > 0 \quad \text{(at the left of the MPP)}, \tag{3.12}$$

$$I + V\frac{dI}{dV} < 0 \quad \text{(at the right of the MPP)}. \tag{3.13}$$

Once the maximum power point is calculated with this method, the controller of the dc-dc converter regulates PV modules' output voltage towards the obtained reference voltage by adjusting the converter's duty ratios. The detailed flow chart of this control method is provided in Fig. 3.3. As indicated in Fig. 3.3, a tolerance (ε) which is equal to zero is used for these criteria in the simulation study because this tolerance (ε) allows the PV module controller to remain at the MPP once it reaches the MPP of the PV system. Otherwise, the PV system may oscillate around the MPP when it reaches MPP, thus producing steady-state error at the operating points of the PV system. Practical ways of addressing this issue in real situations [102] have extensively been studied in the past and are out of the scope of this study.

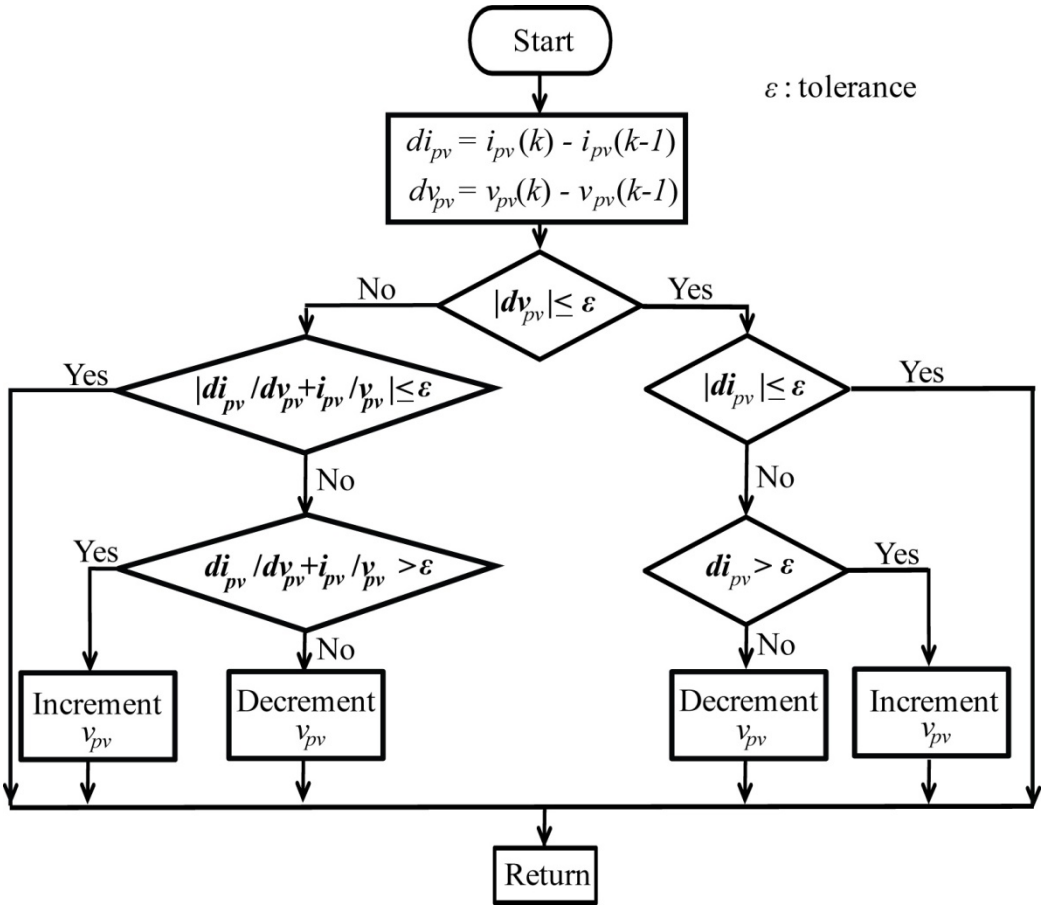

Figure 3.3: Flow chart of the solar maximum power point tracking method (Incremental conductance method) [99], [100], [101].

3.3 RESULTS AND DISCUSSION

Figure 3.4 shows the overall configuration of the simulated 30 kW wind/solar hybrid power system. As this figure suggests, in order to focus on wind energy variations and rapidly changing solar irradiance, this study only considers the simulation of a wind turbine and photovoltaic (PV) modules for the

micro-energy sources of the proposed microgrid. Detailed components inside each building block in Fig. 3.4 are illustrated in Fig. 3.5 to 3.8. As indicated in Fig. 3.5, the wind turbine is modeled by (2.3), (2.4), and (2.5) as discussed in Chapter 2. Detailed specifications of the wind turbine and the permanent magnet synchronous generator (PMSG) model are shown in Tables 3.1 and 3.2 respectively. Figure 3.6 depicts the wind turbine controller developed based on (3.10) and the current mode controller shown in Fig. 3.2. Figure 3.7 illustrates the digital PV module controller that is realized based on the incremental conductance control method discussed in Section 3.2.2. The multiple-input (MI) Ćuk dc-dc converter is modeled with built-in circuit-based components in MATLAB Simulink/Simpowersystems, and the circuit schematic and component values are illustrated in Fig. 3.8. For this study, the internal models of the PMSG and the three-phase rectifier in MATLAB Simulink/Simpowersystems are used. The circuit-based PV model proposed in [92] is used for this simulation study with the parameters presented in the previous Section 2.3.4. In addition, batteries are assumed to be connected to the 380 V_{dc} output stage of the MI Ćuk dc-dc converter in Fig. 3.4 since energy storage devices can be connected to the main dc bus of the proposed microgrid, depicted in Fig. 2.1. Since the main dc bus voltage is fixed and determined by the batteries in Fig. 3.4, the purpose of the controllers for the MI Ćuk converter is to track the maximum power points of each micro-

energy sources in this study. These controllers of which principles are discussed in Section 3.2 are illustrated in Fig. 3.6 and 3.7.

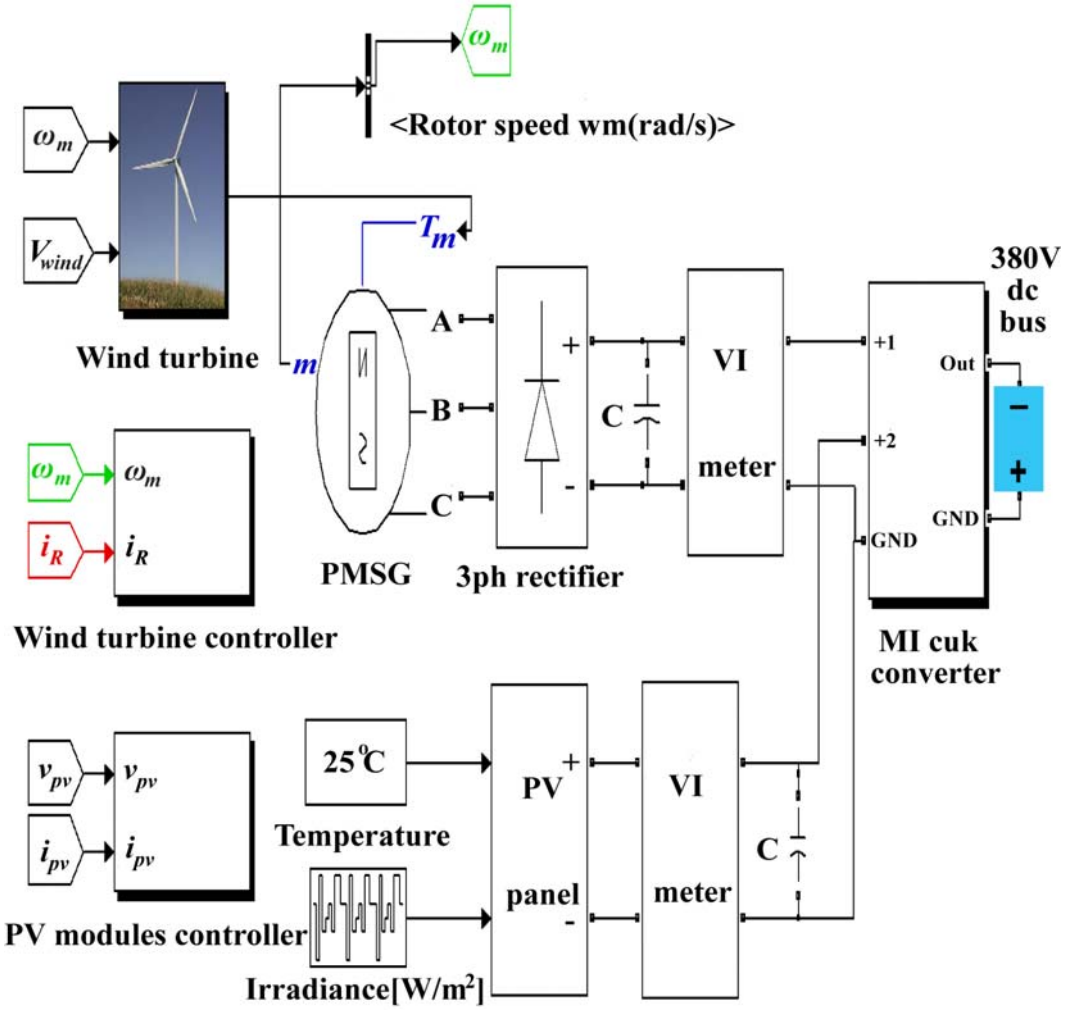

Figure 3.4: Configuration of the simulated 30 kW wind/solar hybrid microgrid.

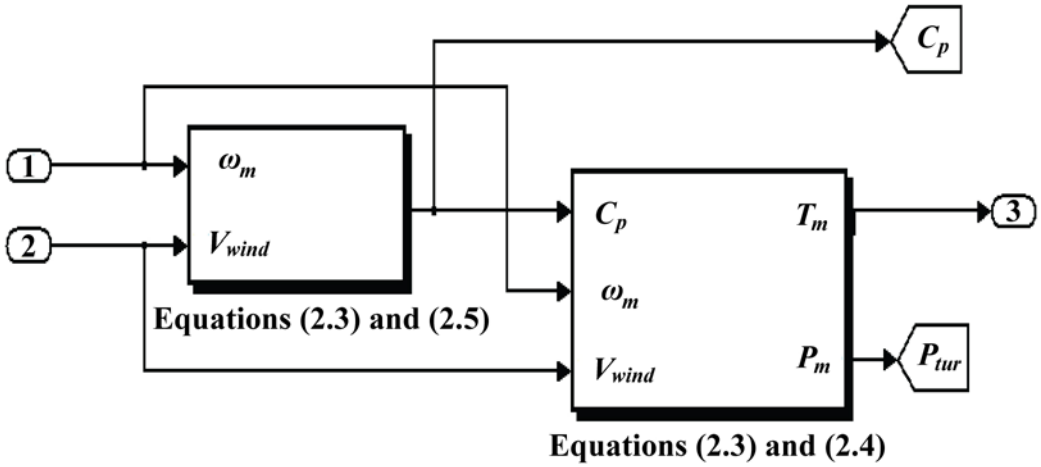

Figure 3.5: Block diagram of the wind turbine in Figure 3.4.

Table 3.1: Parameters and specifications of the wind turbine model in Figure 3.5.

Parameter	Value	Unit
rated power	20	*kW*
rated wind speed	12	*m/s*
rated rotor speed	27.5413	*rad/s*
blade radius	3.7	*M*
blade pitch angle	0	Degree
air density	1.225	kg/m^3

Table 3.2: Specifications of the direct-driven permanent magnet synchronous generator model in Figure 3.4.

Parameter	value	unit
rated power	20	*kW*
rated line voltage	519.6	V_{rms}
stator phase inductance	8.5	*mH*
stator phase resistance	0.05	*Ω*
number of poles	12	
rated mechanical speed	263	*rpm*
electrical base frequency	26.3	*Hz*

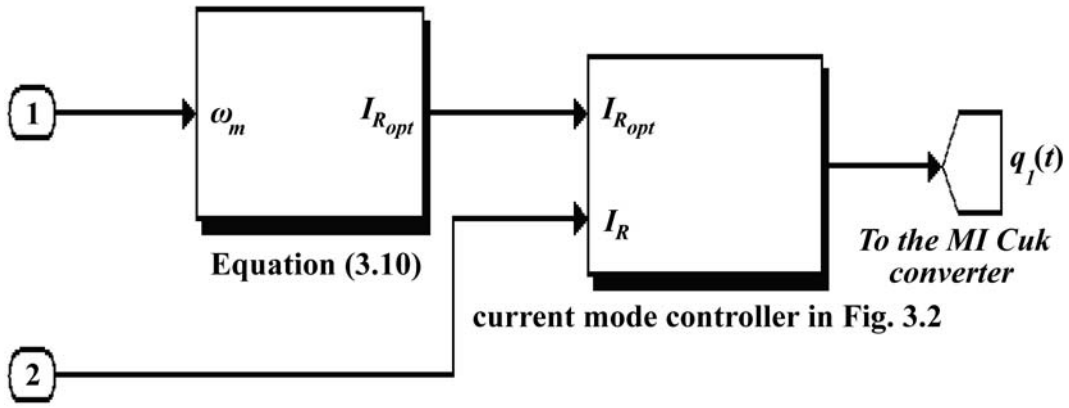

Figure 3.6: Block diagram of the wind turbine controller in Figure 3.4.

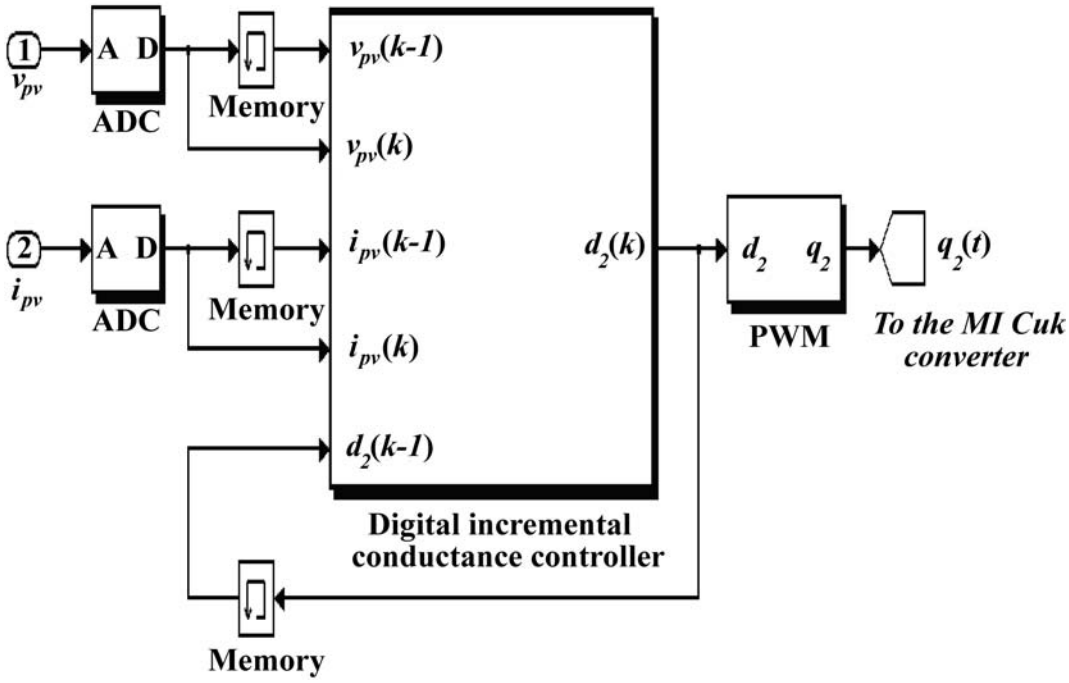

Figure 3.7: Block diagram of the photovoltaic panel controller in Figure 3.4. ADC: Analog-to-digital converter. PWM: Pulse width modulator.

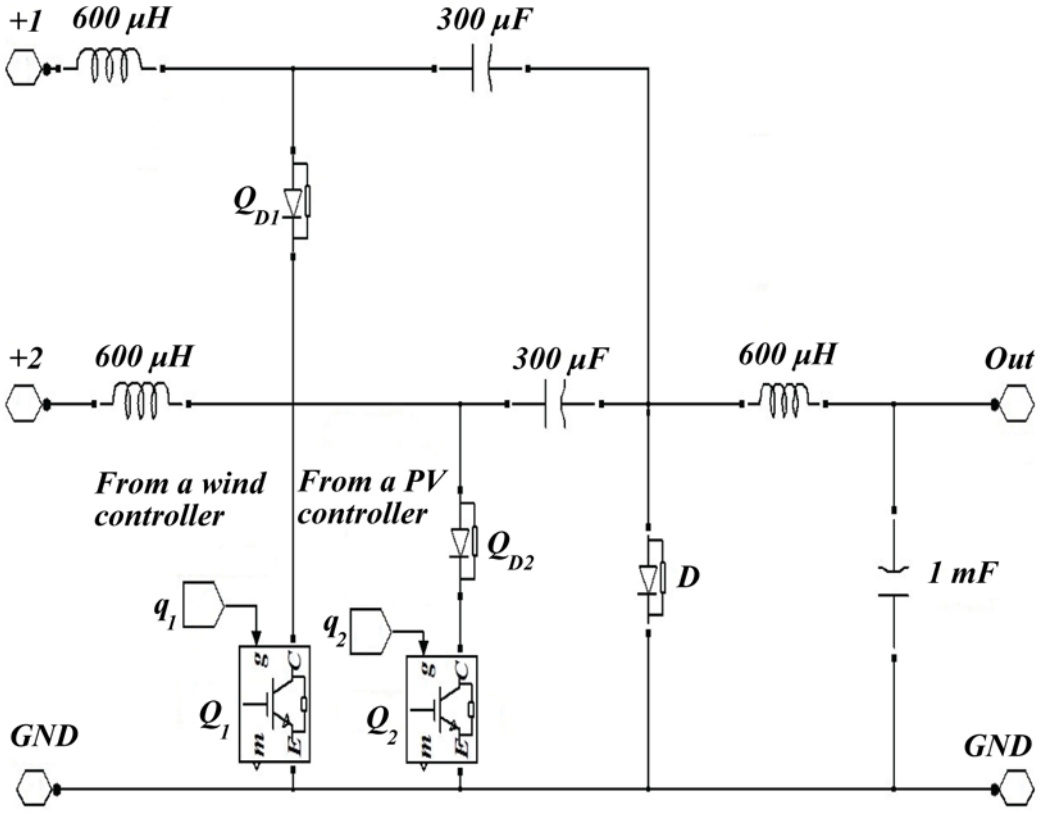

Figure 3.8: Detailed schematic of the multiple-input Ćuk dc-dc converter in Figure 3.4.

Two control blocks in Fig. 3.4, wind turbine and PV panel controllers, are used for harvesting the maximum power from wind and solar energy respectively. The wind turbine controller shown in Fig. 3.6 uses the variable speed control method whose strategy is to operate the wind turbine at the optimal rotor speed ($\omega_{m_{opt}}$) along the optimal power curve below the rated wind speed. On the other hand, this turbine controller uses the target $I_{R_{opt}}$ of the rated wind speed for the

stall regulation above the rated wind speed for the sake of reducing possible damage from mechanical stress and overheating. The other control block in Fig. 3.4, PV panel controller, tracks the maximum power points of solar energy with the incremental conductance method discussed in the previous Section 3.2.2.

3.3.1 Control Performance of the Wind Turbine

In order to illustrate the proposed control strategy in the previous Section 3.2.1, a dynamic wind model presented in Section 2.3.1 is considered to simulate the spatial effect of dynamic wind components such as gusting, rapid ramp changes, and background noises. Figure 3.9 shows the control performance of the wind turbine in the proposed power plant when the dynamic wind model is considered. As indicated in Fig. 3.9(a), 3.9(b), and 3.9(d), when wind speed increases, the wind turbine rotor speed (ω_m) also accelerates so that the output power from the wind turbine (P_{tur}) increases. On the other hand, when wind speed decreases, the wind turbine rotor speed (ω_m) also slows down so that the output power from the wind turbine (P_{tur}) decreases. In addition, the wind turbine is operated at the optimal rotor speed ($\omega_{m_{opt}}$) and harvests the maximum power from wind energy at each wind speed since a rotor power coefficient (C_p) keeps constant at 0.44, which is its maximum possible value as shown in Fig. 3.9(c).

Figure 3.10 shows the output terminal electrical characteristics of the three-phase rectifier with dynamic wind components including gusting, rapid ramp changes, and noises. As shown in Fig. 3.10(a) and 3.10(b), the reference input current ($I_{R_{opt}}$) elevates when wind speed increases. Thus, the rectified output current (I_R) is controlled toward the reference current ($I_{R_{opt}}$), and the terminal rectified output voltage increases as indicated in Fig. 3.10(c). Therefore, the output power from the wind turbine (P_{tur}) elevates when the wind speed also increases. Similarly, when wind speed decreases, the reference input current ($I_{R_{opt}}$) declines, thus decreasing the rectified output current (I_R) and the terminal rectified output voltage as shown in Fig. 3.10(a), 3.10(b), and 3.10(c). Hence, the output power from the wind turbine (P_{tur}) declines when wind speed decreases. Therefore, it can be concluded that the wind generator of this proposed microgrid operates in the optimal power point despite different environmental conditions such as sudden increases or decreases of the wind speed, which likely happen during the day. Moreover, the controller of the wind generator expeditiously reacts to such rapidly changing environmental conditions.

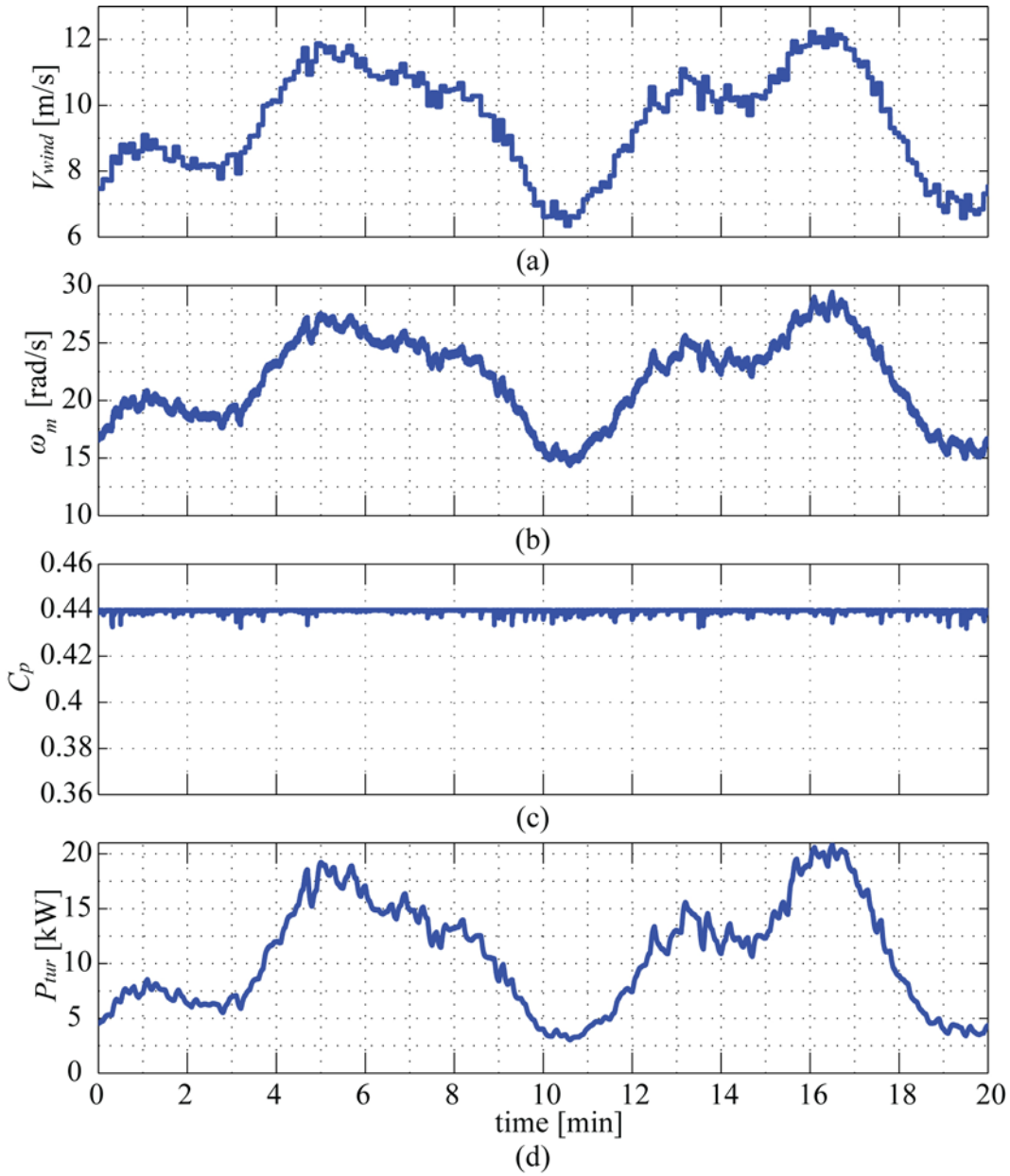

Figure 3.9: Control performance of the wind turbine with wind energy variations. (a) Wind speed (V_{wind}). (b) Wind turbine rotor speed (ω_m). (c) Wind turbine rotor power coefficient (C_p). (d) Wind turbine output power (P_{tur}).

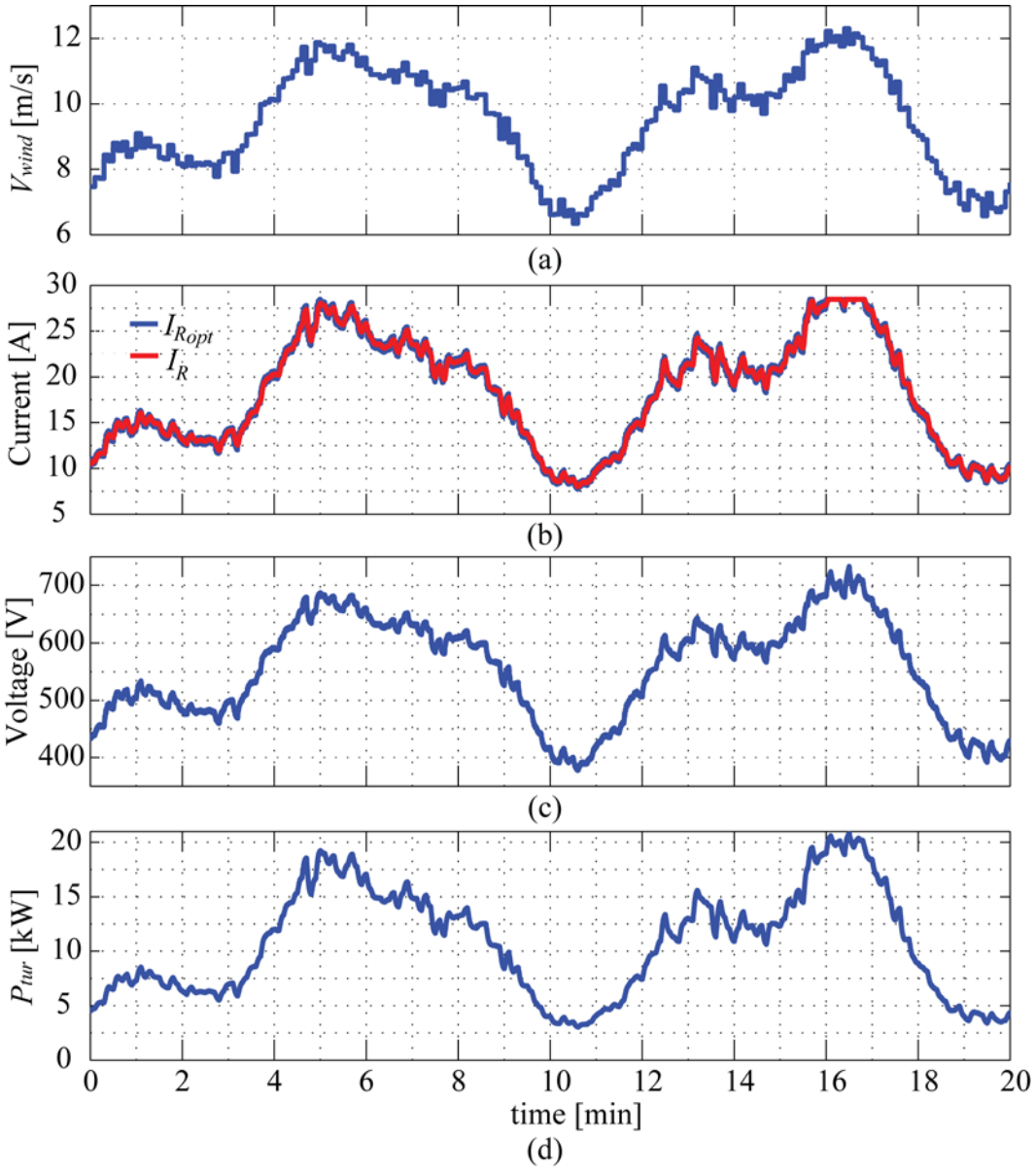

Figure 3.10: Output terminal electrical characteristics of the three-phase rectifier with wind energy variations. (a) Wind speed (V_{wind}). (b) Reference current (I_{Ropt}) and three-phase rectified output current (I_R). (c) Three-phase rectified output voltage (V_R). (d) Wind turbine output power (P_{tur}).

3.3.2 Control Performance of the Photovoltaic Modules

In addition to the dynamic wind model, this study also investigates the dynamics of rapidly changing solar irradiance. The temperature of the PV panel surface is assumed to be fixed at 25ºC during the entire simulation period. Figure 3.11 shows the control performance of PV modules with rapidly changing solar irradiance when dynamic wind components such as gusting, rapid ramp changes, and background noises are considered as shown in Figs. 3.9 and 3.10. As attested in Fig. 3.11, the operating power points of PV modules are well-followed toward the maximum power points because the power output curve tracks the solar irradiance changing curve. Thus, this PV system controller tracks the maximum power points of solar energy regardless of the wind speed variations. Specifically, this PV system controller immediately locates the maximum power point as if the PV system operates without the wind generator. Considering that the performances of these wind and PV controllers illustrated from Fig. 3.9 to Fig. 3.11, it is verified that the discussed control strategy is an adequate one for the proposed wind/solar hybrid microgrid with a multiple-input current-source-interface converter.

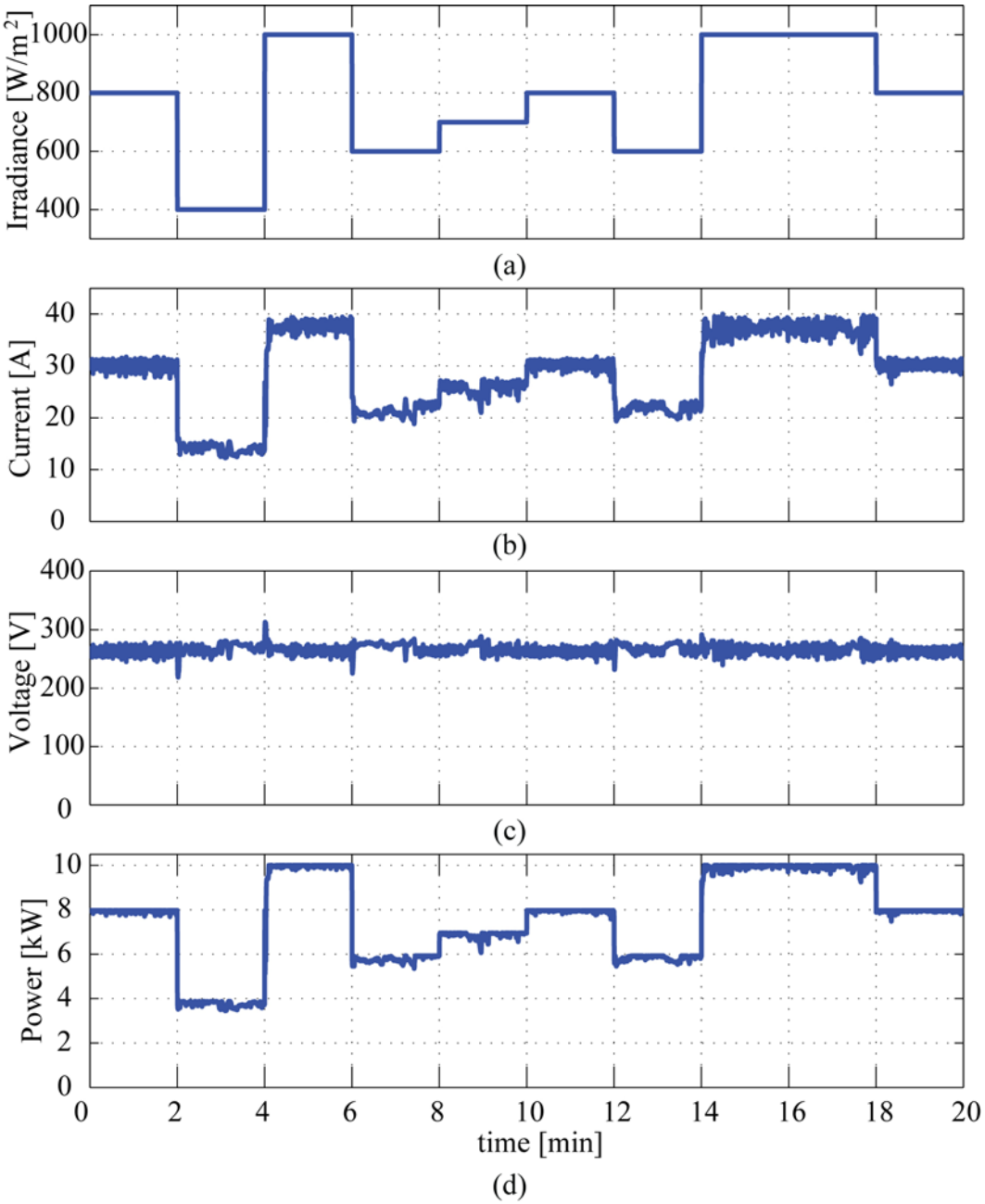

Figure 3.11: Control performance of the PV system. (a) Solar irradiance. (b) PV system's current. (c) PV system's voltage. (d) PV system's power.

3.3.3 Control Performance of the Multiple-input Ćuk Converter

Figure 3.12 shows the control performance of the multiple-input (MI) Ćuk dc-dc converter when wind speed and solar irradiance change in the same manner than in Figs. 3.9 and 3.11 respectively. As depicted in Fig. 3.12(a), the wind generator output power elevates as wind speed increases, while the wind generator output power declines as wind speed decreases. Similarly, the maximum power point of PV modules are tracked upon rapidly changing solar irradiance, as shown in Fig. 3.12(a). These results verify that the wind and PV controller independently locates the optimal operating point of the wind generator and the PV system respectively.

The traces of Fig. 3.12(b) show the input and output power of the MI Ćuk converter. There seem to be differences between the input and output power curves due to the switching and conduction losses in active circuit components, as shown in Fig. 3.8. Figure 3.13 shows the input current waveforms of the MI Ćuk dc-dc converter presented in [38] from a hardware experimental prototype. This hardware experiment suggests that an MI Ćuk dc-dc converter is feasible to combine multiple dc sources with a single converter. In this experiment, two dc sources are combined with an MI Ćuk converter. As attested in Fig. 3.13, the input current waveforms of the MI Ćuk converter are continuous, thus providing operational flexibilities discussed in Section 2.3.5.

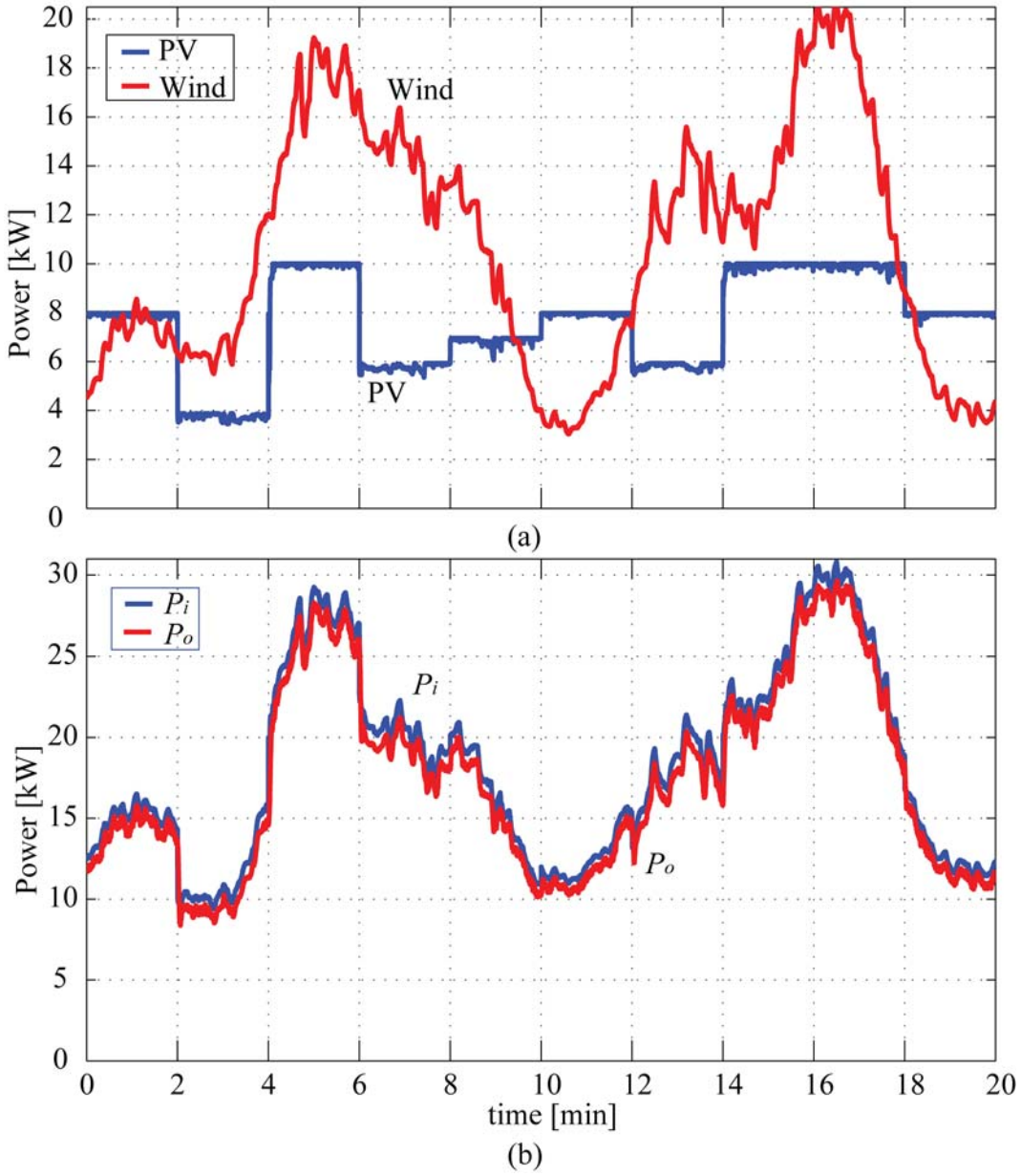

Figure 3.12: Control performance of the MI Ćuk dc-dc converter with wind energy variations and rapidly changing solar irradiance. (a) Wind turbine and PV modules' power. (b) MI Ćuk dc-dc converter input power (P_i) and output power (P_o).

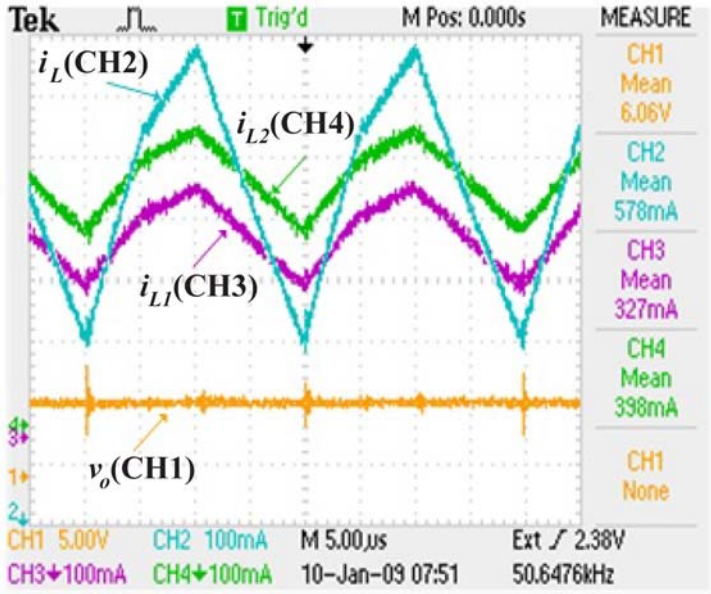

Figure 3.13: Current and output voltage waveforms of the multiple-input Ćuk dc-dc converter.

3.4 CONCLUSION

This chapter presented an operational strategy for a sustainable microgrid presented in Chapter 2. A 30 kW wind/solar hybrid power system dynamic model was developed with MATLAB Simulink/Simpowersystems. The dynamic wind model discussed in Chapter 2 and rapidly changing solar irradiance were considered in the simulation study. For this purpose, this study focused on the maximum power point tracking of the renewable micro-energy sources for the proposed system including a wind turbine and photovoltaic (PV) modules. For the wind generator, this study used a variable speed control method whose strategy is

to capture the maximum wind energy below the rated wind speed. Specifically, an input current control method was used for this variable speed control. In addition, a circuit-based PV model with an incremental conductance control method was used for the simulation study of PV modules. The simulated dynamics in Section 3.3 attested that the control strategy proposed in this chapter is feasible when deploying a wind/solar hybrid power system with a multiple-input current-source-interface dc-dc converter.

Chapter 4

Spatial and Temporal Model of Plug-in Electric Vehicle Charging Demand

4.1 INTRODUCTION

This chapter presents the spatial and temporal model of electric vehicle charging demand for a rapid charging station located near a highway exit. Most previous studies have assumed a fixed charging location and fixed charging time during the off-peak hours for anticipating electric vehicle charging demand. Some other studies have based on limited charging scenarios at typical locations instead of a mathematical model. Therefore, from a distribution system perspective, electric vehicle charging demand is still unidentified quantity which may vary by space and time. In this context, this study proposes a mathematical model of electric vehicle charging demand for a rapid charging station. The mathematical model is based on the fluid dynamic traffic model and the M/M/s queueing

theory. Firstly, the arrival rate of discharged vehicles at a charging station is predicted by the fluid dynamic model. Then, charging demand is forecasted by the M/M/s queueing theory with the arrival rate of discharged vehicles. This mathematical model of charging demand may allow grid's distribution planners to anticipate a charging demand profile at a charging station. A numerical example shows that the proposed model is able to capture the spatial and temporal dynamics of charging demand in a highway charging station.

The rest of this chapter is organized as follows. The detailed highway model in this study is described in Section 4.2. The model formulations of a deterministic fluid model and a stochastic model are discussed in Section 4.3. A numerical example is included in Section 4.4 in order to illustrate spatial and temporal dynamics captured by the proposed charging demand model for a rapid charging station. Section 4.5 concludes with a summary of findings.

4.2 HIGHWAY MODEL DESCRIPTION

In order to provide the context for the analysis here, this section describes a highway for the fluid traffic model modified from the highway Poisson-Arrival-Location Model (PALM) [75]-[77]. This modified highway model here is called herein the highway electric vehicle (EV) PALM so as to differentiate it from the highway PALM [75]-[77] in wireless communication network studies. Figure 4.1

depicts the basic highway model here based on a semi-infinite, one-way, single-lane freeway in the highway PALM [75]-[77]. The horizontal line of Fig. 4.1 represents a unidirectional single-lane highway, and a point x indicates a distance along the highway from the spatial origin which is the beginning point of the highway on the left side of Fig. 4.1. In addition, $v(x,t)$ and t represent the velocity field of each vehicle and time, respectively. Charging stations are located on each exit or entrance as illustrated in Fig. 4.1. Since the basic highway model is semi-infinite as shown in Fig. 4.1, the highway location space is defined as the interval $[0, \infty)$. In order to ensure that the basic highway is unidirectional, the velocity field of each vehicle is assumed to be greater than zero (i.e., $v(x,t) \geq 0$), for all x and t with $x \geq 0$ and $-\infty \leq t \leq \infty$ as depicted in Fig. 4.1. This study also postulates that a vehicle arrives at each entrance of the highway with the Poisson distribution; however, after the vehicle enters the highway, it is assumed to move according to the deterministic function of space and time based on its velocity field as the highway PALM [75]-[77] assumed. Despite this postulation, the highway model still captures stochastic behaviors as well as deterministic behaviors of vehicles according to the highway PALM [75]-[77].

This fundamental highway model can also be used as the building block for a multiple-lane highway in Fig. 4.2 and a bidirectional highway model in Fig. 4.3 as elucidated in [77]. As illustrated in Fig. 4.2, a multiple-lane highway traffic

model is constructed by combining basic highway models in which vehicles have different velocities. As depicted in Fig. 4.3, a bidirectional highway traffic model is built by combining two independent unidirectional highway models with reverse-directional traffic flow; velocities of all vehicles on the bottom highway model in Fig. 4.3 are eastbound (i.e., $v_e(x,t)\geq 0$), while velocities of all vehicles on the top highway model in Fig. 4.3 are westbound (i.e., $v_w(x,t)\geq 0$). Figure 4.4 illustrates a more elaborate highway network which can be developed by superimposing groups of these multiple-lane and bidirectional highways according to [77].

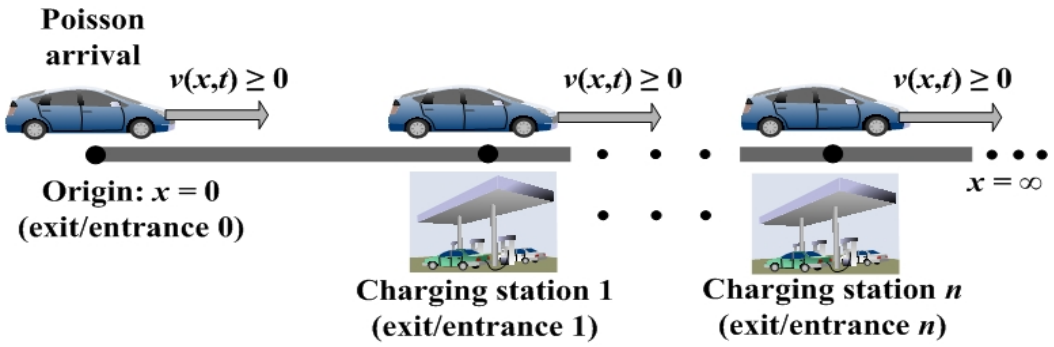

Figure 4.1: Fundamental model of the highway EV PALM.

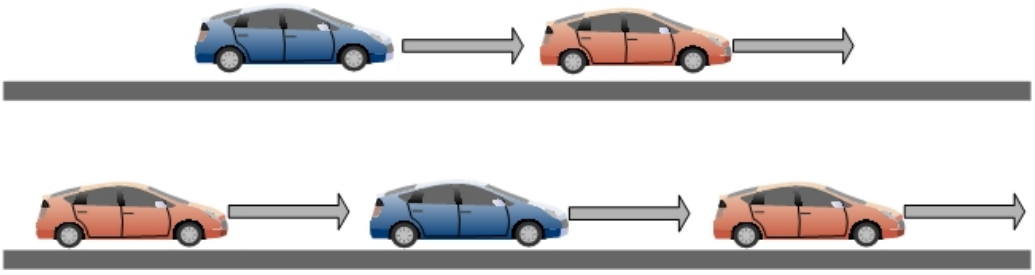

Figure 4.2: Multiple-lane highway model of the highway EV PALM [77].

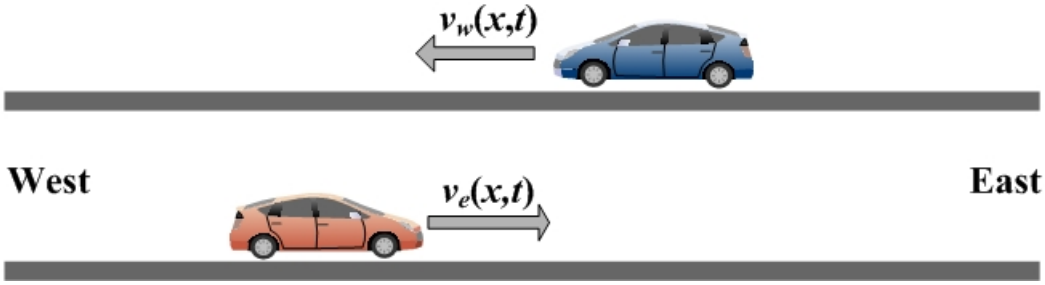

Figure 4.3: Bidirectional highway model of the highway EV PALM [77].

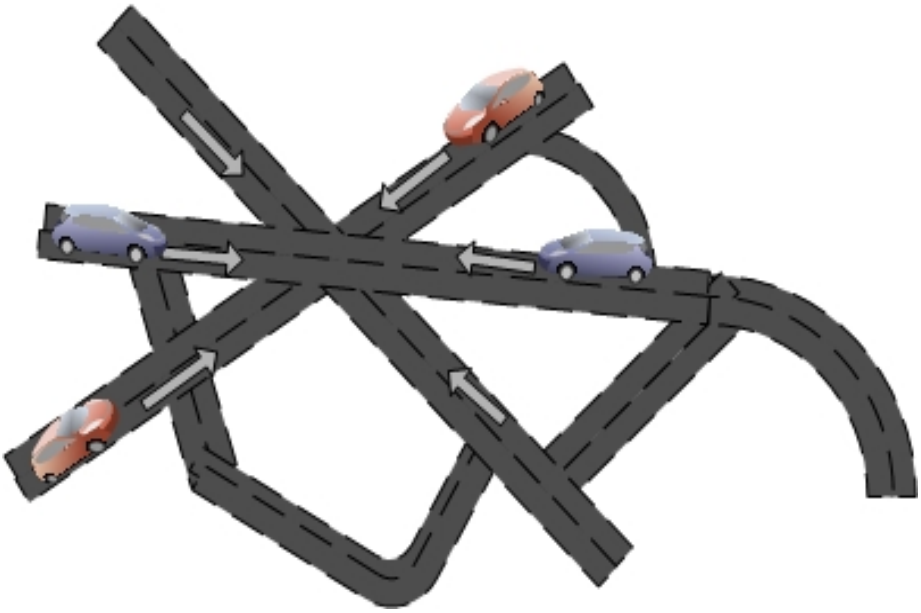

Figure 4.4: Elaborate highway network model of the highway EV PALM [77].

4.3 Model Formulations

As briefly discussed in the Introduction, the first step to calculate EV charging demand is to identify the arrival rate of discharged EVs at a charging station based on the fluid traffic theory [75]-[77]. In Section 4.3.1, a deterministic

fluid dynamic model is presented, which will be used to estimate the arrival rate of discharged EVs at a charging station. This deterministic fluid model is based on the conservation equation of traffic flow, which will be used for drawing Partial Differential Equations (PDEs) whereby general engineering problems can be solved. In Section 4.3.2, EV charging demand will be calculated by the M/M/s queueing theory with the arrival rate of discharged EVs. In Section 4.3.3, a stochastic charging demand model is discussed, which illustrates the expected EV charging demand.

This study assumes that

1) batteries for an already charged vehicle entering the highway have a full state-of-charge (e.g., due to the night-time charging at home) and
2) fully charged batteries can last for the entire range of the trip, which for typical trips it is a short one [54], [55]. Hence, the user of an EV that enters the highway fully charged EV may exit the highway not because the batteries are discharged but rather because he/she may require to rest.

Therefore, in this study it is considered that an already charged vehicle entering the highway does not require visiting a fast charging station during the trip. In contrast, a discharged vehicle on a highway denotes an EV of which batteries are almost drained, thus requiring charging at the closest charging station. In other words, this study focuses on the discharged EV's user who does

not charge at night, thus requiring visiting a charging station on a highway. Before elucidating the highway EV PALM, the definitions for the random variables used in this section and that are represented in Figs. 4.5 (a) and (b) are summarized as follows:

1) $R(x,t)$: The number of discharged EVs remaining in the interval $(0, x]$ at time t

2) $H_d(x,t)$: The number of discharged EVs that have already passed through the position x before time t

3) $F_d^+(x,t)$: The number of discharged EVs that have entered the highway along the interval $(0, x]$ before time t

4) $F_d^-(x,t)$: The number of discharged EVs that have exited the highway along the interval $(0, x]$ before time t

As illustrated in Fig. 4.5(a), $R(x,t)$ represents a static view of the highway status in terms of discharged vehicles within a location interval $(0, x]$ at a given time t. In contrast, Fig. 4.5(b) depicts traffic flow of discharged vehicles during the time interval $(-\infty, t]$. Specifically, $H_d(x,t)$ denotes the number of discharged vehicles which have already passed through the position x before the time t. $F_d^+(x,t)$ and $F_d^-(x,t)$ denote respectively the influx and efflux of discharged vehicles along the interval $(0, x]$ before the time t. In other words, $F_d^+(x,t)$ indicates the number of discharged vehicles which have entered the highway

through any entrances between the highway starting point and a position indicated by x before time t. $F_d^-(x,t)$ is analogous to $F_d^+(x,t)$, but $F_d^-(x,t)$ indicates instead the number of discharged vehicles which have left the highway between those same highway markers before time t. In this context, discharged EVs leaving the system (i.e., $F_d^-(x,t)$) are divided into

1) discharged EVs that permanently depart from the highway and that are recharged at their final destinations which are close to the highway exit and, of course, it is not the highway charging station; or

2) discharged EVs which temporarily leave the highway in order to recharge their batteries at the highway exit charging station. These discharged vehicles which will return to the highway after recharging their batteries at the highway charging station.

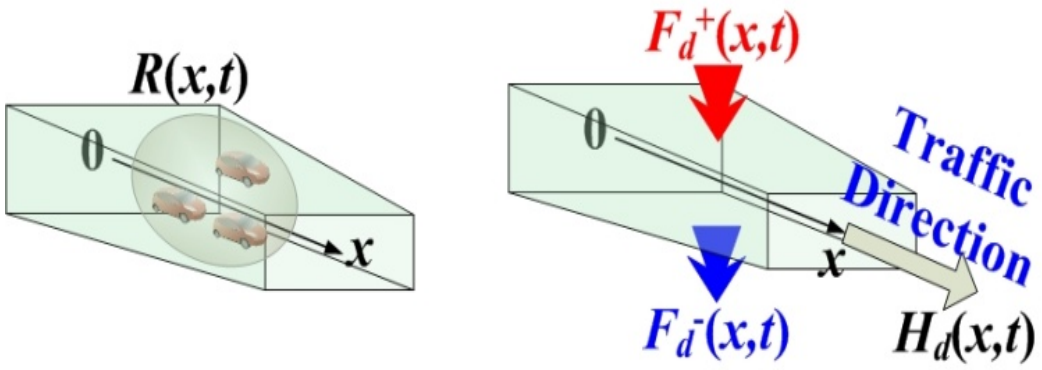

Figure 4.5: Representation of the four variables of discharged vehicles considered in the analysis. (a) Left: $R(x,t)$. (b) Right: $H_d(x,t)$, $F_d^+(x,t)$, $F_d^-(x,t)$.

4.3.1 Deterministic Fluid Dynamic Model

Based on the illustration in Fig. 4.5 and the assumption that all vehicles only move toward the right side, the net flux of discharged vehicles in the interval (0, x] before time t equals the sum of the following quantities: 1) all discharged EVs remaining in location (0, x] at time t (i.e., $R(x,t)$) and 2) all discharged EVs which have passed through the position x before the time t (i.e., $H_d(x,t)$). This equality can be summarized as the following equation, called the conservation equation:

$$R(x,t) + H_d(x,t) = F_d^+(x,t) - F_d^-(x,t). \tag{4.1}$$

If all random variables in (4.1) are assumed to be finite and differentiable in both space and time, the density of discharged vehicles at location x and time t is $r(x,t)$, defined as follows:

$$r(x,t) \equiv \frac{\partial R(x,t)}{\partial x}. \tag{4.2}$$

In the same way, the traffic flow of discharged vehicles at location x and time t is $h_d(x,t)$, defined by

$$h_d(x,t) \equiv \frac{\partial H_d(x,t)}{\partial t}. \tag{4.3}$$

Similarly, the densities of discharged vehicles entering or leaving the highway at location x and time t are respectively $f_d^+(x,t)$ or $f_d^-(x,t)$. That is,

$$f_d^+(x,t) \equiv \frac{\partial^2 F_d^+(x,t)}{\partial x \partial t} \quad \text{and} \quad f_d^-(x,t) \equiv \frac{\partial^2 F_d^-(x,t)}{\partial x \partial t}. \tag{4.4}$$

Based on the definitions in (4.2) to (4.4), the following PDE can be obtained by partially differentiating both sides of the conservation equation (4.1) with respect to the location x and time t:

$$\frac{\partial r(x,t)}{\partial t} + \frac{\partial h_d(x,t)}{\partial x} = f_d^+(x,t) - f_d^-(x,t). \tag{4.5}$$

According to the fundamental law of traffic flow in traffic theory [103], traffic flow can be defined as the multiplication of a traffic density by a vehicle's velocity. Thus, the traffic flow of discharged vehicles at location x and time t, $h_d(x,t)$, can be calculated with multiplying the density of discharged vehicles, $r(x,t)$, by the discharged EVs' velocity at location x and time t, $v(x,t)$. That is,

$$h_d(x,t) = r(x,t)v(x,t). \tag{4.6}$$

By substituting this traffic flow into (4.5), the differential form of the conservation equation can be obtained as follows:

$$\frac{\partial r(x,t)}{\partial t} + \frac{\partial}{\partial x}[r(x,t)v(x,t)] = f_d^+(x,t) - f_d^-(x,t). \tag{4.7}$$

This PDE (4.7) is analogous to the law of conservation of mass in fluid dynamics [104]. In order to simplify (4.7), it can be considered that the velocity field $v(x,t)$ is defined as the time derivative of the location $x(t)$ which is a function of time t as follows:

$$v(x,t) = \frac{dx(t)}{dt}. \tag{4.8}$$

Next, the following equation can be obtained based on the chain rule:

$$\frac{d[r(x,t)]}{dt} = \frac{\partial[r(x,t)]}{\partial t} + \frac{\partial[r(x,t)]}{\partial x}\frac{dx(t)}{dt}. \tag{4.9}$$

By replacing the first time partial derivative in (4.7) with (4.8) and (4.9), the following simplified equation can be obtained:

$$\frac{d[r(x,t)]}{dt} + \frac{\partial v(x,t)}{\partial x} r(x,t) = f_d^+(x,t) - f_d^-(x,t). \tag{4.10}$$

As briefly discussed at the beginning of this section, discharged EVs entering the highway (i.e., $F_d^+(x,t)$) denote discharged EVs which actually arrive at the highway. In contrast, discharged EVs leaving the highway (i.e., $F_d^-(x,t)$) are subdivided into discharged EVs which permanently depart from the system to their final destination different from the highway charging station, and discharged EVs which temporarily leave the highway for recharging their batteries at the highway charging station. Hence, the following notations are provided for further discussions.

1) $B_d^+(x,t)$: All discharged EVs actually arriving at the highway in the interval (0, x] before time t. Thus, $F_d^+(x,t)$ and $B_d^+(x,t)$ are equivalent variables.

2) $B_d^-(x,t)$: All discharged EVs permanently departing from the highway in the interval $(0, x]$ before time t

3) $C_d^-(x,t)$: All discharged EVs temporarily leaving the highway in order to recharge their batteries in the interval $(0, x]$ before time t

In other words, $B_d^+(x,t)$ and $B_d^-(x,t)$ denote arriving and permanently departing discharged EVs, and their densities can be defined as follows:

$$b_d^+(x,t) \equiv \frac{\partial^2 B_d^+(x,t)}{\partial x \partial t} \quad \text{and} \quad b_d^-(x,t) \equiv \frac{\partial^2 B_d^-(x,t)}{\partial x \partial t}. \tag{4.11}$$

These rate densities can be identified with the actual arrival rate (i.e., $\alpha_i(t)$) and the permanent departure rate (i.e., $\beta_i(t)$) of discharged EVs at the ith highway entrance/exit and at time t typically measured in the number of vehicles per minute. The condition, which discharged vehicles can only arrive at and depart from the highway through entrances/exits, can be expressed with a dirac delta function (i.e., $\delta(x)$) as follows [76]:

$$b_d^+(x,t) = f_d^+(x,t) = \sum\nolimits_i \alpha_i(t)\delta(x - y_i), \tag{4.12}$$

$$b_d^-(x,t) = \sum\nolimits_i \beta_i(t)\delta(x - y_i), \tag{4.13}$$

where y_i is a distance from the spatial origin to the ith highway entrance/exit. For simplicity, $\alpha_i(t)$ and $\beta_i(t)$ are assumed here to be constant values. However, in the future, as EV penetration increases and historical data of their use become available, more complex forms for $\alpha_i(t)$ and $\beta_i(t)$ can be considered.

On the other hand, $C_d^-(x,t)$ indicates discharged EVs that have temporarily left the highway for visiting the charging station in the interval (0, x] before time t. The density associated to $C_d^-(x,t)$ can be defined by

$$c_d^-(x,t) \equiv \frac{\partial^2 C_d^-(x,t)}{\partial x \partial t}. \tag{4.14}$$

This temporarily departing discharged EVs' density can be characterized based on the temporarily departing rate per minute (i.e., $\lambda(x,t)$) and the density of discharged EVs (i.e., $r(x,t)$). If it is assumed that discharged EVs will return to the highway immediately after finishing to recharge their batteries, then,

$$c_d^-(x,t) = r(x,t)\lambda(x,t). \tag{4.15}$$

The temporary departing rate per minute (i.e., $\lambda(x,t)$), at which discharged vehicles temporarily leave the highway to recharge their batteries, can be defined with the dirac delta function as:

$$\lambda(x,t) = \sum_i \mu_o(t)\delta(x - y_i). \tag{4.16}$$

Similar to the role played in (4.12) and (4.13), $b_d^+(x,t)$ and $b_d^-(x,t)$, the dirac delta function is included in the temporary departing rate in order to represent that discharged vehicles can only be recharged at a charging station located near the ith exit of the highway. The charging completion rate per minute (i.e., $\mu_o(t)$) can be approximated to a function of the average charging power per vehicle (i.e., p_{av}

[kW]) and the average recharged state-of-charge per vehicle at a charging station (i.e., soc_{av} [kWh]), and that is

$$\mu_o(t) = k_1 \frac{p_{av}}{soc_{av}}, \tag{4.17}$$

where k_1 is a proportional constant that equals 1 over 60 [hour/minute]. The time to complete charging an EV can also be defined as the reciprocal of the charging completion rate.

In summary, the densities of discharged vehicles which enter or leave the system at exits between the origin and location x and at time t—that is, $f_d^+(x,t)$ and $f_d^-(x,t)$, respectively—can be expressed with (4.12) and (4.15) as follows:

$$f_d^+(x,t) = b_d^+(x,t), \tag{4.18}$$

$$f_d^-(x,t) = b_d^-(x,t) + c_d^-(x,t) = b_d^-(x,t) + r(x,t)\lambda(x,t). \tag{4.19}$$

By substituting the right sides of (4.10) with (4.18) and (4.19), the following simplified equation can be derived:

$$\frac{d[r(x,t)]}{dt} = b_d^+(x,t) - b_d^-(x,t) - \left[\frac{\partial v(x,t)}{\partial x} + \lambda(x,t)\right] r(x,t). \tag{4.20}$$

Because of the partial derivative of $v(x,t)$ with respect to x, (4.20) is considered an ordinary differential equation (ODE) if and only if $v(x,t)$ is not a function of $r(x,t)$. Therefore, (4.20) can be solved with numerical methods without much difficulty. The solution of (4.20) is the density of discharged vehicles at

location x and time t, $r(x,t)$. In order to obtain the boundary condition for (4.20), the following points are considered:

1) There does not exist discharged EVs permanently leaving from the spatial origin of the highway but exist discharged EVs entering the spatial origin because the basic highway model is semi-infinite.
2) Since the arrival rate of discharged EVs at the spatial origin (i.e., $\alpha_0(t)$ [number of vehicles per minute]) can be considered the traffic flow at the spatial origin, $\alpha_0(t)$ can be estimated with (4.6). That is,

$$\alpha_0(t) = r(0,t)v(0,t). \tag{4.21}$$

Hence, the boundary condition for $r(0,t)$, for all $t > 0$, is given by

$$r(0,t) = \frac{\alpha_0(t)}{v(0,t)}. \tag{4.22}$$

Next, the solution of $r(x,t)$ from (4.20) can be used to calculate the exiting traffic flow of discharged EVs at the ith exit at time t (i.e., $h_d(y_i,t)$) based on (4.6). The exiting traffic at the ith exit at time t can be considered the sum of the permanent and temporary departing discharged EV. Thus, the arrival rate of discharged EVs at the ith highway charging station (i.e., $z(y_i,t)$) can be considered the difference between $h_d(y_i,t)$ and $\beta_i(t)$, that is

$$z(y_i,t) = h_d(y_i,t) - \beta_i(t) = r(y_i,t)v(y_i,t) - \beta_i(t), \tag{4.23}$$

assuming that discharged EVs depart from the highway exit at the same velocities as were on the highway. Therefore, the arrival rate of discharged vehicles at a charging station can be obtained with the solution of (4.20) (i.e., $r(x,t)$), the exiting speed of discharged EVs at location y_i and time t (i.e., $v(y_i,t)$), and the permanent departing rate at ith exit (i.e., $\beta_i(t)$).

4.3.2 EVs' Charging Demand by the M/M/s Queueing Theory

The next step is to estimate the EVs' charging demand at a rapid charging station with (4.23) and the M/M/s queueing theory [78]. A queue is a waiting line which we may encounter at a bank, a post office, or a grocery store. In this case, EV users are customers in the charging station, and they may require waiting at a charging station in order to recharge their batteries. As illustrated in Fig. 4.6, the following conditions are assumed in the highway charging station:

1) Discharged vehicles arrive at a charging station based on the Poisson distribution whose mean is $z(y_i,t)$.
2) There are s identical charging pumps in the highway charging station under study.
3) The charging completion rate whose mean is $\mu_0(t)$ as described in (4.17) is independently and exponentially distributed.

4) The discharged vehicles form a single queue on their arrivals, which will be charged by the next available charging pump based on a first-come-first-served rule.

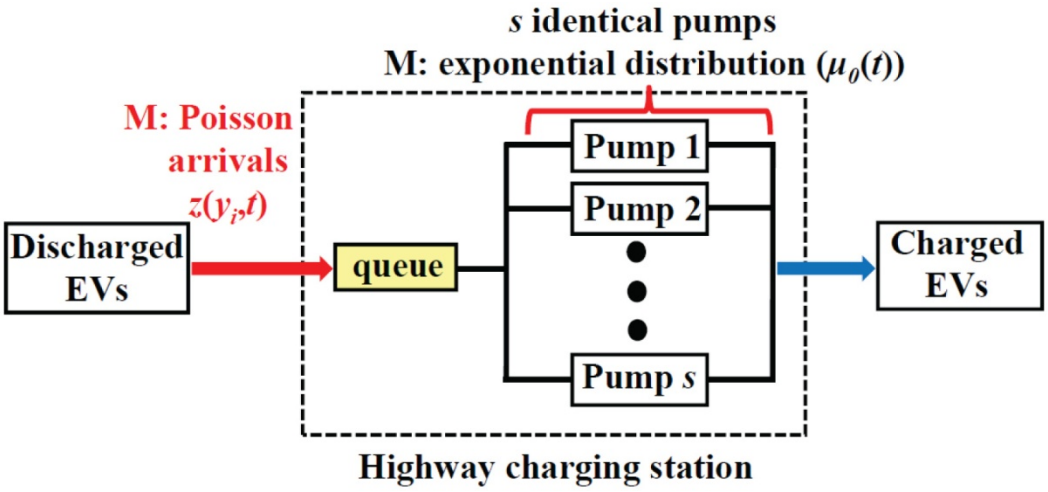

Figure 4.6: M/M/s queueing system in the highway charging station.

These assumptions allow an EV charging service at a fast charging station to follow the M/M/s queueing theory. According to the M/M/s queueing theory [78], the queueing system is stable if and only if the occupation rate of charging pumps (i.e., ρ) is less than 1. This occupation rate of charging pumps denotes the probability that a charging pump is not inactive (i.e., it is in use), and it can be obtained by dividing the arrival rate of discharged EVs at a charging station (i.e., $z(y_i,t)$) by the number of charging pumps in a charging station (i.e., s) and by the charging completion rate (i.e., $\mu_0(t)$). That is [78],

$$\rho = \frac{z(y_i, t)}{s\mu_0(t)}. \tag{4.24}$$

Based on the necessary and sufficient condition for the stability of the queueing system and (4.24), the minimum number of charging pumps should meet the following inequality in order to ensure that the queueing system of the highway charging station is stable [78]:

$$s > \frac{z(y_i, t)}{\mu_0(t)}. \tag{4.25}$$

Next, the limiting-state probability (i.e., $Q_n(t)$) that there are n numbers of discharged EVs in the highway charging station is required to determine the expected number of busy charging pumps. According to [78], the limiting-state probability that there are n number of customers—that is, the number of discharged EVs— in the M/M/s queueing system is given by

$$Q_n(t) = \begin{cases} \dfrac{1}{n!}\left(\dfrac{z(y_i, t)}{\mu_0(t)}\right)^n Q_0 & if\ 0 \le n \le s-1 \\ \dfrac{1}{s!s^{n-s}}\left(\dfrac{z(y_i, t)}{\mu_0(t)}\right)^n Q_0 & if\ n \ge s \end{cases}, \tag{4.26}$$

where Q_0 equals

$$Q_0 = \left[\sum_{n=0}^{s-1}\frac{1}{n!}\left(\frac{z(y_i, t)}{\mu_0(t)}\right)^n + \frac{1}{s!}\left(\frac{z(y_i, t)}{\mu_0(t)}\right)^s\left(\frac{s\mu_0(t)}{s\mu_0(t) - z(y_i, t)}\right)\right]^{-1}. \tag{4.27}$$

Since n and s are the number of discharged EVs and charging pumps in the highway charging station, respectively, the number of busy charging pumps is given by min(n,s). Then, the expected number of busy charging pumps (i.e., $B(t)$) is defined by [78] as

$$B(t) = \sum_{n=0}^{\infty} \min(n,s) Q_n(t) = \frac{z(y_i,t)}{\mu_0(t)}. \quad (4.28)$$

Derivation of (4.26) to (4.28) is out of the scope of this chapter. However, a reader may refer to [78] for an explanation of such equations.

Now, the power demand of the ith exit charging station (i.e., $P_d(y_i,t)$) can be estimated by the multiplication of the average charging power per pump (i.e., p_{av}) and the expected number of busy charging pumps (i.e., $B(t)$). That is, the charging demand is

$$P_d(y_i,t) = p_{av} B(t) = p_{av} \frac{z(y_i,t)}{\mu_0(t)}, \quad (4.29)$$

where y_i is a distance from the spatial origin to the ith exit on the highway.

4.3.3 Stochastic Model

The purpose of the stochastic highway EV PALM presented here is to identify the expected value of the stochastic EV charging demand. As the deterministic fluid dynamic model in Section 4.3.1, the same highway environment and notations are used here for the stochastic model unless stated

otherwise. Thus, the same conservation equation can be applied to the stochastic highway EV PALM as follows:

$$R(x,t)+H_d(x,t)=F_d^+(x,t)-F_d^-(x,t). \tag{4.30}$$

Similar to the highway PALM [75]-[77], the density and traffic flow of discharged vehicles at location x and time t—that is, $\langle r(x,t)\rangle$ and $\langle h_d(x,t)\rangle$, respectively—in the stochastic model should be expressed with the expected values of discharged vehicles so that the model reflects stochastic behaviors of discharged vehicles on a highway. That is,

$$\left\langle r(x,t)\right\rangle \equiv \frac{\partial E[R(x,t)]}{\partial x} \quad \text{and} \quad \left\langle h_d(x,t)\right\rangle \equiv \frac{\partial E[H_d(x,t)]}{\partial t}, \tag{4.31}$$

where $E[\cdot]$ indicates the expectation of the operand. In order to capture stochastic behaviors, the densities, $\langle f_d^+(x,t)\rangle$, $\langle f_d^-(x,t)\rangle$, $\langle b_d^+(x,t)\rangle$, $\langle b_d^-(x,t)\rangle$, and $\langle c_d^-(x,t)\rangle$ should similarly be defined by

$$\left\langle f_d^+(x,t)\right\rangle \equiv \frac{\partial^2 E[F_d^+(x,t)]}{\partial x\partial t}, \quad \left\langle f_d^-(x,t)\right\rangle \equiv \frac{\partial^2 E[F_d^-(x,t)]}{\partial x\partial t},$$

$$\left\langle b_d^+(x,t)\right\rangle \equiv \frac{\partial^2 E[B_d^+(x,t)]}{\partial x\partial t}, \quad \left\langle b_d^-(x,t)\right\rangle \equiv \frac{\partial^2 E[B_d^-(x,t)]}{\partial x\partial t},$$

$$\text{and} \quad \left\langle c_d^-(x,t)\right\rangle \equiv \frac{\partial^2 E[C_d^-(x,t)]}{\partial x\partial t}. \tag{4.32}$$

In the stochastic model, discharged EVs randomly enter the highway at location x and time t with the mean rate of $\langle \alpha_i(t)\rangle$, while discharged EVs

randomly depart from and then never return to the highway with the mean rate of $\langle\beta_i(t)\rangle$. Then, similar to (4.12) and (4.13), $\langle f_d^+(x,t)\rangle$, $\langle b_d^+(x,t)\rangle$, and $\langle b_d^-(x,t)\rangle$ are expressed with $\langle\alpha_i(t)\rangle$ and $\langle\beta_i(t)\rangle$

$$\left\langle b_d^+(x,t)\right\rangle = \left\langle f_d^+(x,t)\right\rangle = \sum_i \left\langle \alpha_i(t)\right\rangle \delta(x-y_i)\,, \tag{4.33}$$

$$\left\langle b_d^-(x,t)\right\rangle = \sum_i \left\langle \beta_i(t)\right\rangle \delta(x-y_i)\,. \tag{4.34}$$

With the mean temporarily departing rate $\langle\lambda(x,t)\rangle$, discharged EVs randomly leave the highway to charge their batteries. Then, similar to (4.15) and (4.16), the associated density (i.e., $\langle c_d^-(x,t)\rangle$) is given by

$$\left\langle c_d^-(x,t)\right\rangle = \left\langle r(x,t)\right\rangle\left\langle \lambda(x,t)\right\rangle = \left\langle r(x,t)\right\rangle \sum_i \left\langle \mu_o(t)\right\rangle \delta(x-y_i)\,, \tag{4.35}$$

where $\langle\mu_o(t)\rangle$ is analogous to (4.17) and given by

$$\left\langle \mu_o(t)\right\rangle = k_1 \frac{p_{av}}{soc_{av}}\,. \tag{4.36}$$

With these definitions, the mean density of discharged vehicles at location x and time t (i.e., $\langle r(x,t)\rangle$) can be obtained by solving the following ODE, similar to (4.20):

$$\frac{d\left\langle r(x,t)\right\rangle}{dt} = \left\langle b_d^+(x,t)\right\rangle - \left\langle b_d^-(x,t)\right\rangle - \left[\frac{\partial v(x,t)}{\partial x} + \left\langle \lambda(x,t)\right\rangle\right]\left\langle r(x,t)\right\rangle\,. \tag{4.37}$$

In the same manner of (4.22), the boundary condition for $\langle r(0,t)\rangle$, for all $t > 0$, is given by

$$\langle r(0,t)\rangle = \frac{\langle \alpha_0(t)\rangle}{v(0,t)}. \tag{4.38}$$

Then, $<r(x,t)>$ can be obtained by solving (4.37) with (4.38), and the mean arrival rate of discharged EVs at the ith exit charging station (i.e., $<z(y_i,t)>$) can be considered the difference between the expected exiting traffic flow at location y_i and time t (i.e., $<h_d(y_i,t)>$) and the mean rate of $<\beta_i(t)>$, similar to (4.23). That is,

$$\langle z(y_i,t)\rangle = \langle h_d(y_i,t)\rangle - \langle \beta_i(t)\rangle = \langle r(y_i,t)\rangle v(y_i,t) - \langle \beta_i(t)\rangle. \tag{4.39}$$

By applying the mean arrival rate of discharged EVs into the M/M/s queueing theory [78], the expected charging demand of the ith exit charging station (i.e., $E[P_d(y_i,t)]$) can be estimated by

$$E[P_d(y_i,t)] = p_{av}\frac{\langle z(y_i,t)\rangle}{\langle \mu_0(t)\rangle}, \tag{4.40}$$

which is similar to (4.29).

4.4 Numerical Example and Discussions

This section provides a numerical example in order to illustrate the spatial and temporal dynamics of the highway EV PALM presented in Section 4.3. A numerical example of the stochastic model is presented here because planning activities will typically be based on such model. Nevertheless, extension into the deterministic model is straightforward because both models are analogous, as

demonstrated by (4.20) and (4.37) showing the same form. Likewise, (4.29) and (4.40) show that the expected charging demand in the stochastic model and the charging demand in the deterministic model are also analogous.

For the sake of simplicity, the example provided here assumes

1) that two entrances/exits are located one at the spatial origin and the other at 5 km from the spatial origin, respectively,
2) that discharged vehicles arrive to the spatial origin and to the 5 km entrance at the mean rate of 3 vehicles/min (indicated by $<\alpha_0(t)> = <\alpha_1(t)> = 3$), and
3) that only one rapid charging station is located near the exit at 5km as shown in Fig. 4.7.

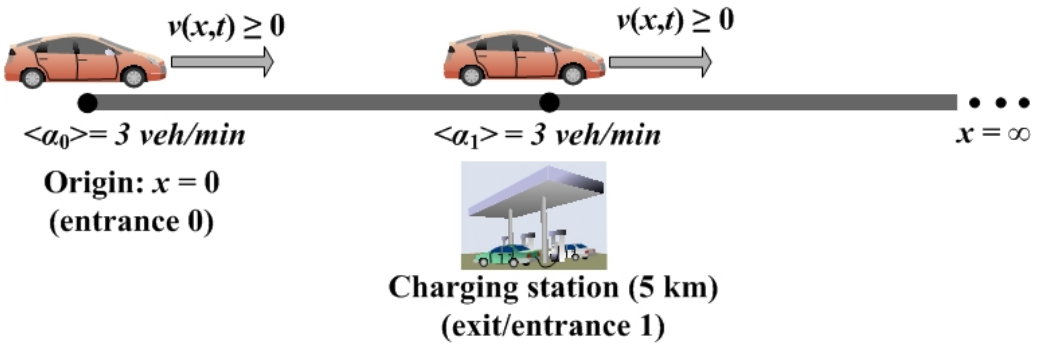

Figure 4.7: Basic highway model for a numerical example.

In addition, it is postulated that discharged vehicles only depart from the highway through the 5 km exit in order to recharge their batteries at a rapid charging station. Although standards of charging power for a rapid charging station have not been finalized yet, it is expected that an EV can be charged with 50 to 70 kW at a level 3 charging station [13]. In this example, it is assumed that an EV will be charged with 70 kW at the highway fast charging station (i.e., p_{av}=70 kW). The EV considered here is a PHEV33 compact sedan [19] whose electric mode driving range and battery size are 33 mile—that is, about 53 km—and 8.6 kWh, respectively. Since the EV user may also recharge it at the final destination (e.g., office), every user will not fully charge it at the highway charging station whose charging price may be more expensive than that of the slow charging station (e.g., home or office). Thus, it is assumed that the average charge per vehicle at the highway charging station (i.e., soc_{av}) is 4 kWh which is about 50 % of the battery capacity and can last for the one-way trip to the final destination. Then, the mean charging completion rate per minute (i.e., $<\mu_o(t)>$) can be calculated by (4.36), which results equal to 0.3. Hence, it requires 3.4 minutes to charge 4 kWh with a 70 kW charging rate.

In order to mimic traffic congestion during rush hour, it is hypothesized in this example that the velocity fields of vehicles on the highway $v(x,t)$ is 1 km/min

for all $x \geq 0$ when $t \leq 40$ or $t > 55$ min and that $v(x,t)$ during the time interval (40, 55] min corresponding to rush hour is described as follows:

$$v(x,t) = \begin{cases} 1 & \text{if } x \leq 3 \\ 1-0.6(x-3) & \text{if } 3 < x \leq 4 \\ 0.4 & \text{if } 4 < x \leq 6 \\ 0.4+0.6(x-6) & \text{if } 6 < x \leq 7 \\ 1 & \text{if } x \geq 7 \end{cases}. \tag{4.41}$$

Figure 4.8 depicts the velocity fields of vehicles on a highway as a function of the distance from the spatial origin during the time interval (40, 55] min representing rush hour. As can be seen in Fig. 4.8, vehicles on a highway reduce their velocities starting from 3 km and then recover their normal speeds at 7 km. The velocity drop in the interval (3, 7] during the time interval (40, 55] min in Fig. 4.8 can represent reduced speeds in a congested area during rush hour.

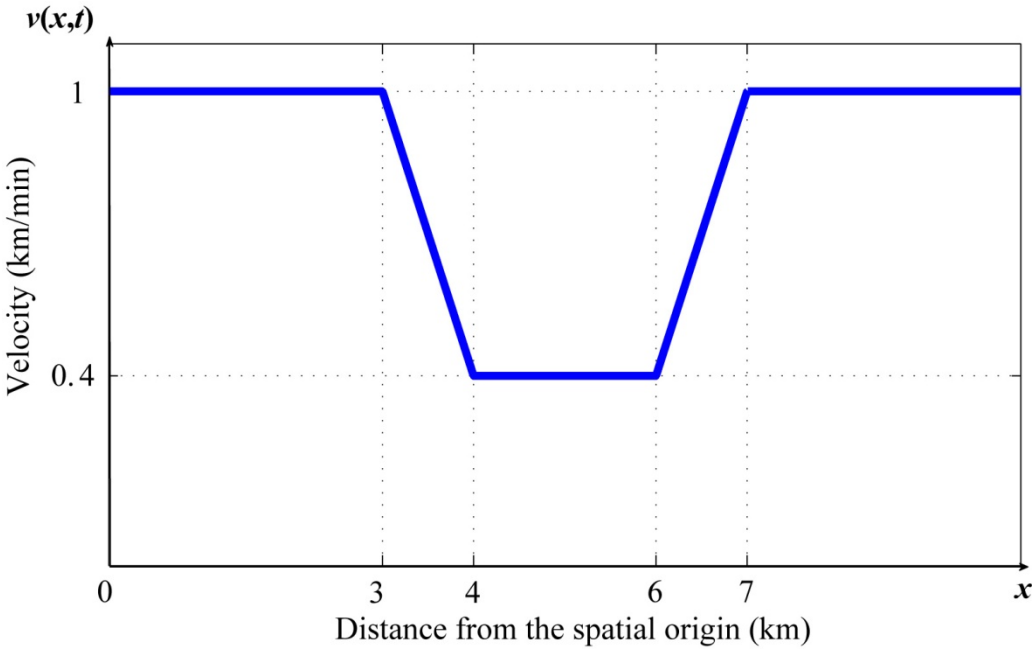

Figure 4.8: Velocity fields of vehicles on a highway during the time interval (40, 55] min.

Under those aforementioned assumptions and parameters of this example, the mean traffic density of discharged vehicles on a highway is solved with numerical methods using (4.37) during normal hours and rush hour. The boundary condition for $<r(0,t)>$ is $<\alpha_0(t)>/v(0,t)$ for all $t > 0$ as obtained from (4.38). Figures 4.9 and 4.10 illustrate the simulated mean densities of discharged vehicles on a highway at t = 35 min and t = 45 min respectively. As revealed by Fig. 4.9, the mean density of discharged vehicles is constant at 3 vehicles/min, which is the same than the boundary condition. This result indicates that during the normal

hours if the mean rate of discharged vehicles entering the highway is constant the expected EV charging demand at a highway charging station is almost constant. In contrast, as attested in Fig. 4.10, the simulated mean density of discharged vehicles during the rush hour—the time interval (40, 55] min—increases sharply starting from 3 km due to reduced velocities in the interval (3, 7]. This high mean traffic density in these locations implies that there is traffic congestion in this area and that the expected EV charging demand of a rapid charging station located near the 5 km exit increases due to the high mean density of discharged vehicles in this region. Figures 4.11 and 4.12 obtained by (4.6) describe the simulated mean traffic flow of discharged vehicles on a highway at t = 35 min and t = 45 min respectively. Assuming that the EV charging service is followed by the M/M/s queueing theory, the expected charging demand of the 5 km charging station can be predicted by (4.39) and (4.40) as can be seen in Fig. 4.13. Since it is assumed that discharged EVs only depart for visiting the charging station, there is no permanent departing discharged EV traffic at the 5 km exit in this example (i.e., $<\beta_1(t)> = 0$ at the 5 km exit). The expected charging demand during the time interval (40, 55] min was 2.42 times greater than that during the normal hours due to traffic congestion as indicated in Fig. 4.13. In addition, based on (4.25) and considering that the time intervals (40, 55] min in this example represents the worst scenario during the day in which traffic jams occur at this location, at least

25 charging pumps should be prepared at this charging station to cope with the demand.

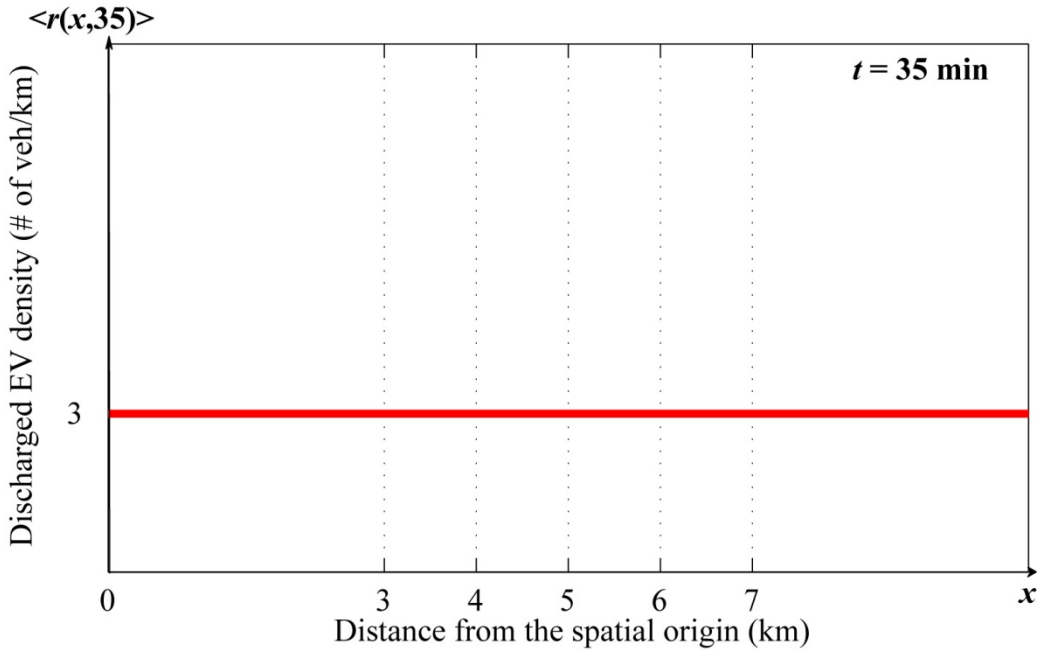

Figure 4.9: Simulated mean density of discharged vehicles at t = 35 min.

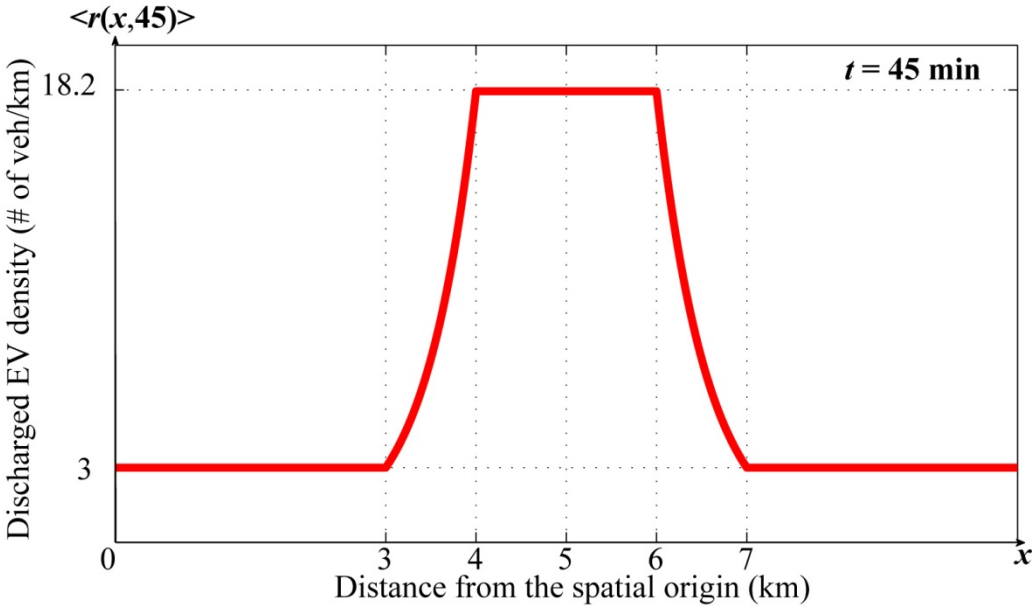

Figure 4.10: Simulated mean density of discharged vehicles at t = 45 min.

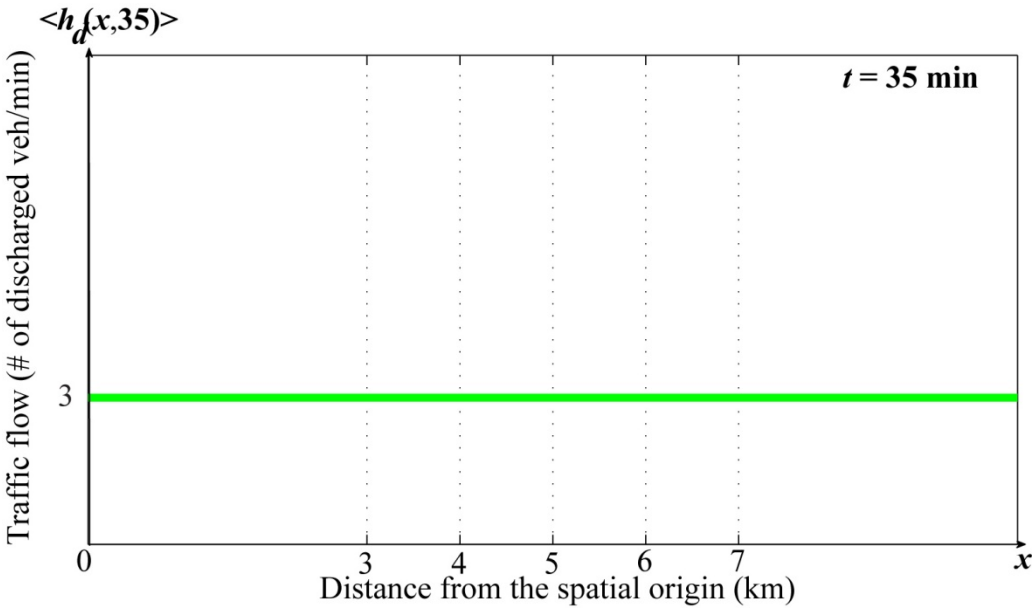

Figure 4.11: Simulated mean traffic flow of discharged vehicles at t = 35 min.

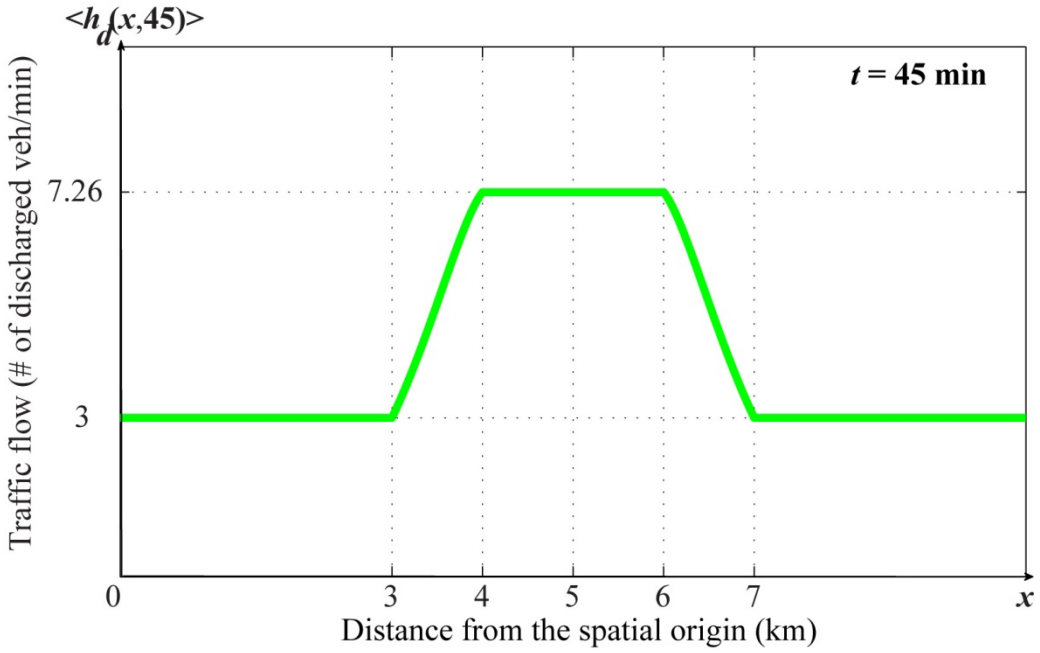

Figure 4.12: Simulated mean traffic flow of discharged vehicles at t = 45 min.

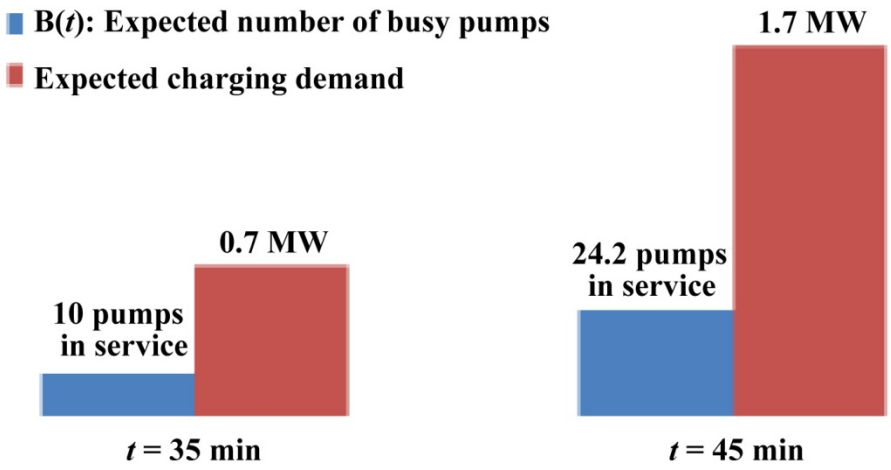

Figure 4.13: Expected Number of charging pumps in service and expected charging demand at the 5 km fast charging station on a highway.

4.5 CONCLUSION

This chapter proposed a mathematical model of EV charging demand for a rapid charging station on a highway. This mathematical model can help to identify EV charging demand which varies by space and time. The charging demand model is based on the fluid traffic model in wireless communication studies [75]-[77] and the M/M/s queueing theory [78]. Specifically, the first step is to identify the arrival rate of discharged EVs at a charging station with the highway EV PALM. This highway EV model is modified from the fluid traffic model [75]-[77] so that an EV user can charge the EV only at a charging station located near a highway exit. Secondly, EV charging demand is calculated with the arrival rate of discharged EVs by the M/M/s queueing theory [78]. As described in Section 4.2, a basic model of the highway EV PALM (i.e., a semi-infinite, unidirectional, single-lane model) is presented for a fundamental building block by which elaborate highway networks can be developed.

EVs change utility distribution planning approach in many ways but a significant change is the following: traditionally, distribution planners only require focusing on local demand or on demand within the domain of the electric utility. With EVs, demand may move from another utility into the area of the utility for which the planner works. Thus, distribution planning is no longer local but may, actually, require coordination among neighboring utilities. The proposed

model may help distribution planners to coordinate each other since a numerical example provided here showed that the proposed model is able to capture the spatial and temporal dynamics of charging demand at a highway charging station. Hence, it can be concluded that the proposed spatial and temporal model may help distribution utility planners to identify charging demand for a specific highway charging station and may allow city and rural planners to determine the location and size of a rapid charging station on a highway.

The proposed charging demand model can also facilitate computer implementation of the planning or analysis tool for the distribution system of the highway charging station because it consists of an ODE which can be solved by a difference equation using a digital computer. Moreover, this model requires relatively known traffic data which are traffic velocities and the number of vehicles entering or leaving the highway at a given exit and for a given time. Utility distribution planners may identify these traffic data from GPSs or CCTVs on a highway and from demographic data.

Chapter 5

Sustainable Microgrid with Flexible Charging Strategies for a Rapid Charging Station

5.1 INTRODUCTION

This chapter presents flexible charging strategies and a sustainable microgrid for a rapid charging station on a highway. As discussed in Chapter 4, the highway electric vehicle (EV) Poisson-Arrival-Location Model (PALM) may allow distribution planners to anticipate an EV charging demand profile at a specific charging station on a highway. Based on this demand profile, distribution planners can consider flexible charging strategies in which they may install energy storage devices in a rapid charging station. These energy storage devices may allow an EV to be charged with a reasonable charging price even during the peak time if they can be charged with inexpensive electricity from the utility grid during the off-peak time or with low-priced and "green" electricity from renewable energy sources. For these flexible charging strategies, the sustainable

microgrid proposed in Chapter 2 is applied to the distribution system of a rapid charging station on a highway. A 2MW wind/solar sustainable power system for this rapid charging station is developed with MATLAB Simulink/ Simpowersystems based on the predicted EV charging demand discussed in Chapter 4.

The rest of this chapter is organized as follows. The flexible charging strategies for a rapid charging station are discussed in Section 5.2. A sustainable microgrid which may enable these flexible charging strategies for the rapid charging station is presented in Section 5.3. Section 5.4 concludes with the summary of findings.

5.2 FLEXIBLE CHARGING STRATEGIES IN A RAPID CHARGING STATION

As the numerical example in Chapter 4 predicts the EV charging demand of a rapid charging station on a highway, the highway EV PALM may allow power system engineers to estimate a charging demand profile for a specific charging station. Based on this demand profile, appropriate distribution systems such as transformers and underground cables can be installed up to the charging station [56]-[58]. In addition, depending on the demand profile, adequate size of energy storage systems can be determined, which will provide flexible energy sources such as renewable energy sources in order to reduce the price of charging

an EV as illustrated in Fig. 5.1. The energy storage system shown in Fig. 5.1 may be charged with inexpensive electricity from the utility grid during the off-peak hours or with low-priced and "green" electricity from renewable energy sources such as wind and solar energy. This energy storage system may provide electricity for charging batteries of EVs with a reasonable price during the peak hours as depicted in Fig. 5.2. The charging station may also participate in a demand response program [79]-[83] in this way. Moreover, this charging demand model may allow city planners to determine the geographical location and size of a rapid charging station on a highway depending on the charging demand profile. Furthermore, this EV charging demand model requires relatively known traffic data which are traffic velocities and the number of vehicles entering or leaving the highway at a given exit and for a given time. The former traffic data can be collected through GPSs or CCTVs on a highway without much difficulty [84]-[87], and the latter data can be estimated with demographic data.

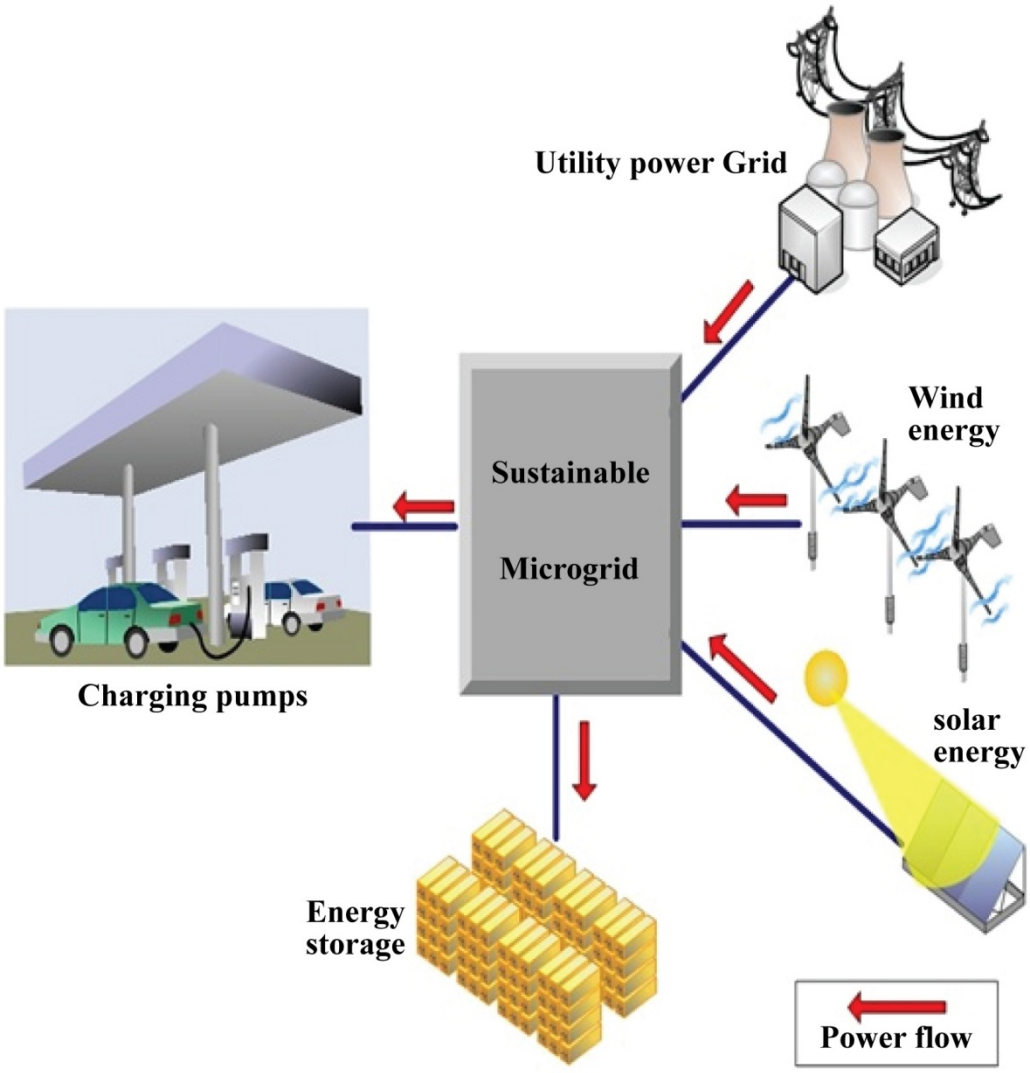

Figure 5.1: Flexible charging strategy in a rapid charging station during the off-peak time.

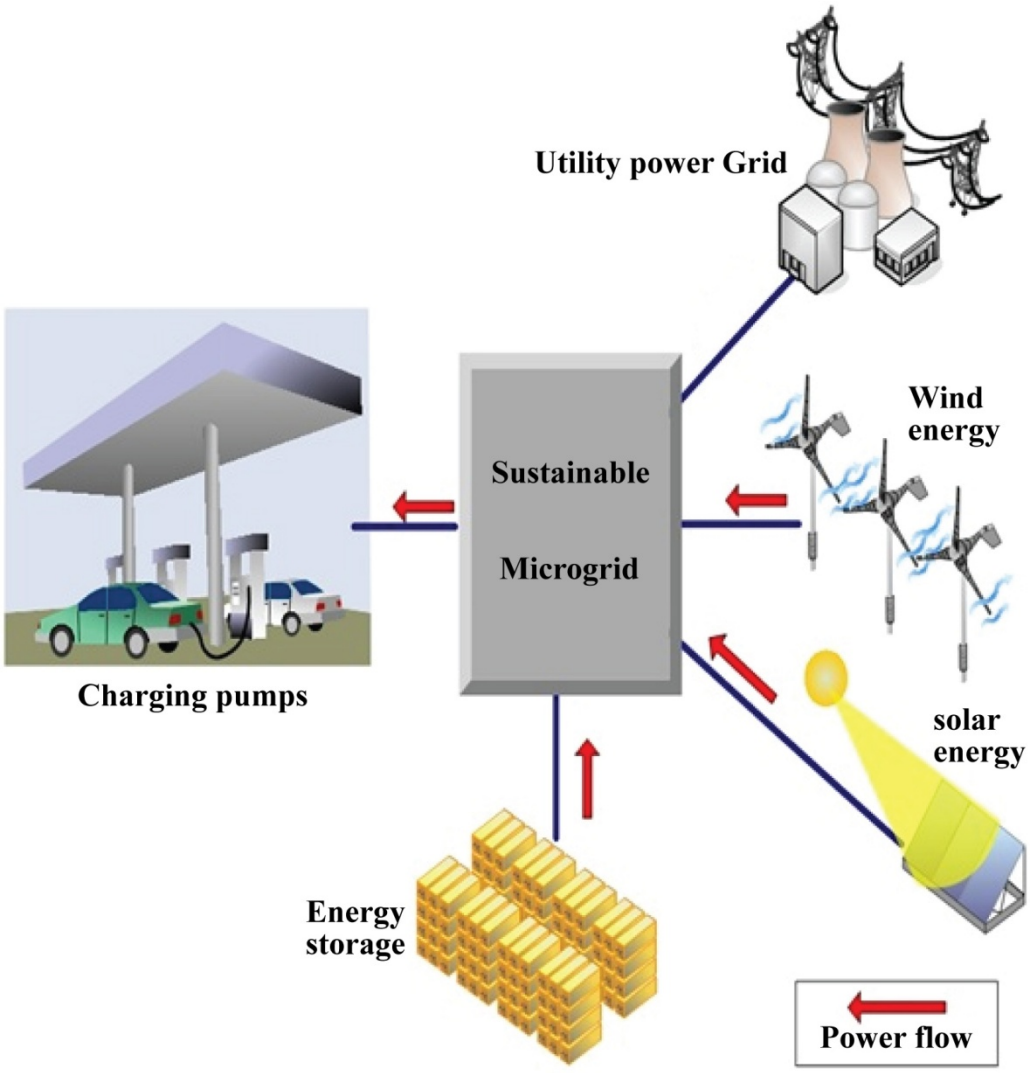

Figure 5.2: Flexible charging strategy in a rapid charging station during the peak time.

5.3 SUSTAINABLE MICROGRID FOR A RAPID CHARGING STATION

The dynamic modeling and operational strategy of the sustainable microgrid proposed in Chapter 2 and 3 can be applied to the power system of a rapid charging station shown in Figs. 5.1 and 5.2. Figure 5.3 shows the sustainable microgrid architecture for a rapid charging station with wind and solar energy resources. Although standards of charging voltage and power levels for a rapid charging station have not been determined yet, it is expected that an electric vehicle can be charged with a voltage level of 480 V at a level 3 charging station [13]. Thus, a voltage level of 480 V is considered to be the main dc bus voltage in this power system because electric vehicle charging pumps can be directly connected to the main dc bus. It is also more suitable for bidirectional power flow between the intended microgrid and the utility power grid [22]. In addition, based on results from the numerical example presented in Chapter 4, the base and peak demand of this rapid charging station as shown in Fig. 4.13 are expected to be 0.7 MW and 1.7 MW respectively. It is assumed that the time intervals (40, 55] min in the example represent the worst scenario during the day in which traffic jams occur at this rapid charging station. To cope with this electric vehicle charging demand, a 2 MW wind/solar sustainable power system is considered for this rapid charging station as shown in Fig. 5.3.

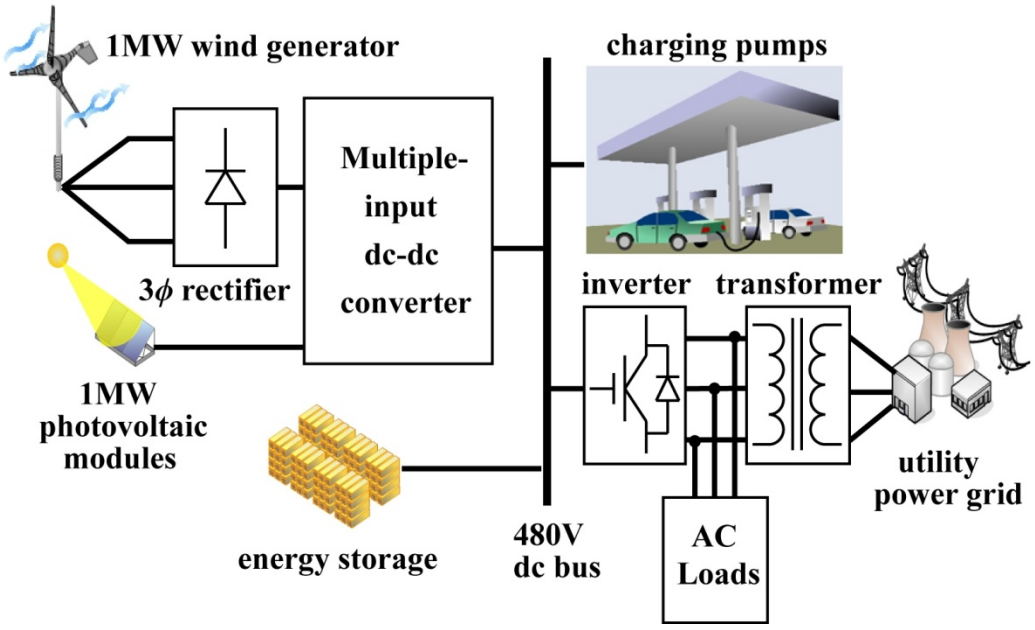

Figure 5.3: Sustainable microgrid architecture of a rapid charging station with wind and solar energy resources.

An 1 MW wind turbine is used for the sustainable microgrid of this rapid charging station shown in Fig. 5.3. Detailed specifications of the wind turbine and the permanent magnet synchronous generator (PMSG) are described in Tables 5.1 and 5.2 respectively. In addition, 1 MW photovoltaic modules are used for the microgrid of this rapid charging station, and detailed specifications of 1 MW photovoltaic modules are explained in Table 5.3. Similar to Chapter 3, this study only focuses the simulations of the wind generator and photovoltaic modules for the micro-sources for this microgrid in order to explore wind energy variations and rapidly changing solar irradiance.

Table 5.1: Parameters and specifications of the wind turbine model in Figure 5.3.

Parameter	value	unit
rated power	1	*MW*
rated wind speed	12	*m/s*
rated rotor speed	3.873	*rad/s*
blade radius	26.14	*m*
blade pitch angle	0	degree
air density	1.225	kg/m^3

Table 5.2: Specifications of the direct-driven permanent magnet synchronous generator model in Figure 5.3.

Parameter	value	unit
rated power	1	*MW*
rated line voltage	1558.8	V_{rms}
stator phase inductance	2.5	*mH*
stator phase resistance	0.005	*Ω*
number of poles	12	
rated mechanical speed	37	*rpm*
electrical base frequency	3.7	*Hz*

Table 5.3: Specifications of PV modules in Figure 5.3.

Parameter	value	unit
total rated power	1	*MW*
rated irradiance	1000	W/m^2
rated temperature	25	*°C*
modules' voltage at the MPP	1315	*V*
modules' current at the MPP	761	*A*
number of series modules	50	
number of parallel modules	100	

Simulation study results based on MATLAB Simulink/Simpowersystems are provided in Fig. 5.4 in order to illustrate the control performance of the sustainable microgrid for this rapid charging station. As depicted in Fig. 5.4 (a), this simulation study uses the wind model that was presented in [90] and that consists of a base wind component, a gusting wind component, a rapid ramp wind component, and background noises. Despite these dynamic wind speed changes, the wind turbine power coefficient maintains its maximum possible value (i.e., 0.44), as depicted in Fig. 5.4 (b). As attested in Figs. 5.4 (c) to 5.4 (e), the wind generator output power elevates when wind speed increases. On the other hand, the wind generator output power declines when wind speed decreases. Hence, it can be concluded that the wind generator of this microgrid operates in the optimal power point despite different environmental conditions such as sudden increases or decreases of the wind speed, which likely happen during the day. In addition, this simulation study also investigates the dynamics of rapidly changing solar irradiance as shown in Fig. 5.4 (a). As attested in Figs. 5.4 (c) to 5.4 (e), the operating power points of PV modules are well-controlled toward the maximum power points because the power output curve tracks the solar irradiance changing curve.

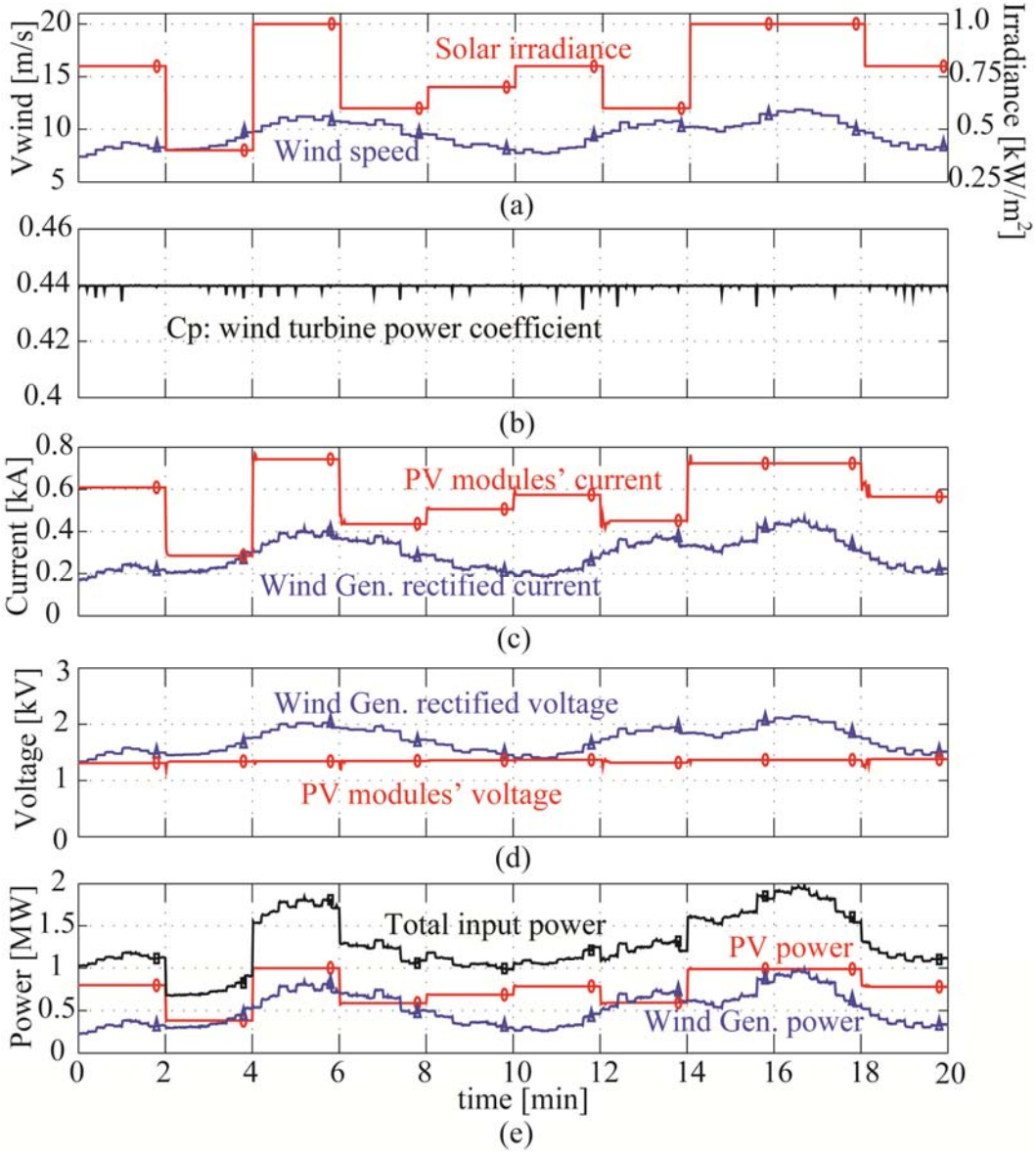

Figure 5.4: Control performance of the sustainable microgrid for a rapid charging station with wind and PV resources. (a)Wind speed and solar irradiance. (b)Wind turbine power coefficient. (c)Wind generator rectified current and PV modules' current. (d)Wind generator rectified voltage and PV modules' voltage. (e)Wind turbine, PV modules, and total renewable energy sources' power.

5.4 CONCLUSION

This chapter presented a sustainable microgrid with flexible charging strategies for a rapid charging station on a highway. The spatial and temporal EV charging demand model discussed in Chapter 4 may help distribution utility planners to identify an EV charging demand profile at a specific charging station on a highway. Based on this demand profile, they can consider flexible charging strategies including using energy storage devices or participating a demand response program [79]-[83]. The sustainable microgrid presented in Chapter 2 was considered for these flexible charging strategies of a rapid charging station on a highway. A 2MW wind/solar sustainable power system for this rapid charging station was developed with MATLAB Simulink/Simpowersystems based on the predicted base and peak EV charging demand discussed in Chapter 4.

Chapter 6

Conclusions

A “smarter grid” is expected to be more flexible and more reliable than traditional electric power grids. For full deployment of the “smarter grid”, various technologies such as advanced autonomous control methods, distributed generation, and plug-in electric vehicles, may be required to be incorporating into the traditional electric power grids. Among these technologies, this dissertation presented a sustainable microgrid and a spatial and temporal model of plug-in electric vehicle (EV) charging demand for the “smarter grid”. This sustainable microgrid can be operated in an “islanded” mode in which it can continue to generate power during natural disasters or grid outages, thus improving disaster resiliency of the “smarter grid” and of the more electric transportation system. In addition, the proposed spatial and temporal EV charging demand model can help to identify the impact of increased transportation electrification on the “smarter grid”.

Chapters 2 and 3 presented the dynamic modeling and operational strategy of a sustainable microgrid primarily powered by wind and solar energy. These renewable sources are integrated into the main bus through multiple-input current-source-interface dc-dc converters. The intended application for such a microgrid is an area in which there is interest in achieving a sustainable energy solution, such as a telecommunication site or a residential area part of a future "smarter grid" power system. Wind energy variations and rapidly changing solar irradiance were considered in this study in order to explore the effect of such environmental variations to the intended microgrid. A 30 kW wind/solar hybrid microgrid dynamic model was developed with MATLAB Simulink/Simpowersystems. The proposed sustainable microgrid is able to reduce additional parallel converters with a multiple-input dc-dc converter. The dynamics of wind and solar energy and the ac modeling of the wind generator were considered in the proposed model in contrast that the previous studies. In addition, the proposed microgrid not only can produce electricity from the renewable energy sources but may also transmit surplus power to the utility grid in normal operation. Moreover, the proposed microgrid can improve disaster resiliency of the "smarter grid" because it can be operated in an islanded mode during natural disaster or grid outages.

In Chapter 4, a mathematical model of electric vehicle (EV) charging demand for a rapid charging station on a highway was presented. This

mathematical model can help to identify EV charging demand which varies by space and time. The charging demand model is based on the fluid traffic model in wireless communication studies [75]-[77] and the M/M/s queueing theory [78]. The proposed spatial and temporal model may help distribution utility planners to identify charging demand for a specific highway charging station so that they coordinate each other. In addition, this EV charging demand model may allow city and rural planners to determine the location and size of a rapid charging station on a highway. The proposed charging demand model can also facilitate computer implementation of the planning or analysis tool for the distribution system of the highway charging station because it consists of an ODE which can be solved by a difference equation using a digital computer. Moreover, this model requires relatively known traffic data which are traffic velocities and the number of vehicles entering or leaving the highway at a given exit and for a given time. Utility distribution planners may identify these traffic data from GPSs or CCTVs on a highway and from demographic data.

Chapter 5 presented a sustainable microgrid with flexible charging strategies for a rapid charging station on a highway. Based on EV charging demand, distribution planners can consider flexible charging strategies including using energy storage devices or participating a demand response program [79]-[83]. The sustainable microgrid presented in Chapter 2 was considered for these

flexible charging strategies of a rapid charging station on a highway. A 2MW wind/solar sustainable power system for this rapid charging station was developed with MATLAB Simulink/Simpowersystems based on the predicted base and peak EV charging demand discussed in Chapter 4.

Bibliography

[1] Litos Strategic Communication, "The Smart Grid: An Introduction," prepared for the U.S. Department of Energy, 2008, pp. 1-43

[2] A. Kwasinski, "Implication of smart-grids development for communication systems in normal operation and during disasters," in *Proc*. 2010 *IEEE INTELEC*, pp. 1-8.

[3] P. L. Joskow, "California's Electricity Crisis," *Oxford Review of Economic Policy,* vol. 17, no. 3, pp. 365-388, Sept. 2001.

[4] G. Andersson, P. Donalek, R. Farmer, N. Hatziargyriou, I. Kamwa, P. Kundur, N. Martins, J. Paserba, P. Pourbeik, J. Sanchez-Gasca, R. Schulz, A. Stankovic, C. Taylor, and V. Vittal, "Causes of the 2003 major grid blackouts in North America and Europe, and recommended means to improve system dynamic performance," *IEEE Trans. Power Syst.,* vol. 20, no. 4, pp. 1922-1928, Nov. 2005.

[5] A. Kwasinski, W. W. Weaver, P. L. Chapman, and P. T. Krein, "Telecommunications Power Plant Damage Assessment for Hurricane Katrina–Site Survey and Follow-Up Results " *IEEE Syst. J.,* vol. 3, no. 3, pp. 277-287, Sept. 2009.

[6] B. Fahimi, A. Kwasinski, A. Davoudi, R. S. Balog, and M. Kiani, "Charge It!," *IEEE Power Energy Mag.,* vol. 9, no. 4, pp. 54-64, Jul.-Aug. 2011.

[7] A. Kwasinski and P. T. Krein, "Multiple-input dc-dc converters to enhance local availability in grids using distributed generation resources," in *Proc*. 2007 *IEEE 22nd APEC*, pp. 1657-1663.

[8] A. Kwasinski, "Quantitative Evaluation of DC Microgrids Availability: Effects of System Architecture and Converter Topology Design Choices," *IEEE Trans. Power Electron.,* vol. 26, no. 3, pp. 835-851, Mar. 2011.

[9] A. Kwasinski, "Telecommunications outside plant power infrastructure: Past performance and technological alternatives for improved resilience to hurricanes," in *Proc*. 2009 *IEEE 31st INTELEC*, pp. 1-6.

[10] A. Kwasinski, "Technology Planning for Electric Power Supply in Critical Events Considering a Bulk Grid, Backup Power Plants, and Micro-Grids," *IEEE Syst. J.,* vol. 4, no. 2, pp. 167-178, Jun. 2010.

[11] A. Kwasinski and P. T. Krein, "Optimal Configuration Analysis of a Microgrid-Based Telecom Power System," in *Proc*. 2006 *IEEE 28th INTELEC*, pp. 1-8.

[12] A. Kwasinski and P. T. Krein, "Telecom power planning for natural and man-made disasters," in *Proc*. 2007 *IEEE 29th INTELEC*, pp. 216-222.

[13] L. Dickerman and J. Harrison, "A New Car, a New Grid," *IEEE Power Energy Mag.,* vol. 8, no. 2, pp. 55-61, Mar.- Apr. 2010.

[14] M. Duvall, E. Knipping, M. Alexander, L. Tonachel, and C. Clark, "Environmental Assessment of Plug-In Hybrid Electric Vehicles - Volume 1: Nationwide Greenhouse Gas Emissions," Electric Power Research Institute, Palo Alto, CA, Tech. Rep. 1015325, 2007.

[15] K. Parks, P. Denholm, and T. Markel, "Costs and Emissions Associated with Plug-In Hybrid Electric Vehicle Charging in the Xcel Energy Colorado Service Territory," National Renewable Energy Laboratory, Golden, CO, Tech. Rep. NREL/TP-640-41410, May 2007.

[16] C. Samaras and K. Meisterling, "Life Cycle Assessment of Greenhouse Gas Emissions from Plug-in Hybrid Vehicles: Implications for Policy," *Environ. Sci. & Tech.,* vol. 42, no. 9, pp. 3170-3176, Apr. 2008.

[17] C. H. Stephan and J. Sullivan, "Environmental and Energy Implications of Plug-In Hybrid-Electric Vehicles," *Environ. Sci. & Tech.,* vol. 42, no. 4, pp. 1185-1190, Feb. 2008.

[18] P. Mohseni and R. G. Stevie, "Electric Vehicles: Holy Grail or Fool's Gold," in *Proc*. 2009 *IEEE PES Gen. Meet.*, pp. 1-5.

[19] M. Kintner-Meyer, K. P. Schneider, and R. G. Pratt, "Impacts Assessment of Plug-in Hybrid Vehicles on Electric Utilities and Regional US Power

Grids: Part 1: Technical Analysis," Pacific Northwest National Laboratory, Richland, WA, Tech. Rep. PNNL-SA-61669, Nov. 2007.

[20] C. K. Nelson, "Plug-in electric vehicle impact on Nashville Electric Service distribution system planning," in *Proc*. 2010 *IEEE Power Eng. Society Transmission and Distribution Conf. and Expo.*, pp. 1-2.

[21] J. Taylor, A. Maitra, M. Alexander, D. Brooks, and M. Duvall, "Evaluations of plug-in electric vehicle distribution system impacts," in *Proc*. 2010 *IEEE PES Gen. Meet.*, pp. 1-6.

[22] A. Kwasinski and P. T. Krein, "A Microgrid-based Telecom Power System using Modular Multiple-Input DC-DC Converters," in *Proc*. 2005 *IEEE 27th INTELEC*, pp. 515-520.

[23] O. H. A. Shirazi, O. Onar, and A. Khaligh, "A novel telecom power system," in *Proc*. 2008 *IEEE 30th INTELEC*, pp. 1-8.

[24] S. Wakao, R. Ando, H. Minami, F. Shinomiya, A. Suzuki, M. Yahagi, S. Hirota, Y. Ohhashi, and A. Ishii, "Performance analysis of the PV / wind / wave hybrid power generation system," in *Proc*. 2003 *3rd World Conf. Photovoltaic Energy Conversion*, pp. 2337-2340 Vol.3.

[25] C. Yaow-Ming, L. Yuan-Chuan, H. Shih-Chieh, and C. Chung-Sheng, "Multi-Input Inverter for Grid-Connected Hybrid PV/Wind Power

System," *IEEE Trans. Power Electron.,* vol. 22, no. 3, pp. 1070-1077, May 2007.

[26] L. Solero, F. Caricchi, F. Crescimbini, O. Honorati, and F. Mezzetti, "Performance of a 10 kW power electronic interface for combined wind/PV isolated generating systems," in *Proc*. 1996 *27th Annual IEEE PESC*, pp. 1027-1032, vol. 2.

[27] B. S. Borowy and Z. M. Salameh, "Dynamic response of a stand-alone wind energy conversion system with battery energy storage to a wind gust," *IEEE Trans. Energy Convers.,* vol. 12, no. 1, pp. 73-78, Mar. 1997.

[28] R. Chedid and S. Rahman, "Unit sizing and control of hybrid wind-solar power systems," *IEEE Trans. Energy Convers.,* vol. 12, no. 1, pp. 79-85, Mar. 1997.

[29] R. Chedid, H. Akiki, and S. Rahman, "A decision support technique for the design of hybrid solar-wind power systems," *IEEE Trans. Energy Convers.,* vol. 13, no. 1, pp. 76-83, Mar. 1998.

[30] W. D. Kellogg, M. H. Nehrir, G. Venkataramanan, and V. Gerez, "Generation unit sizing and cost analysis for stand-alone wind, photovoltaic, and hybrid wind/PV systems," *IEEE Trans. Energy Convers.,* vol. 13, no. 1, pp. 70-75, Mar. 1998.

[31] F. Giraud and Z. M. Salameh, "Steady-state performance of a grid-connected rooftop hybrid wind-photovoltaic power system with battery storage," *IEEE Trans. Energy Convers.,* vol. 16, no. 1, pp. 1-7, Mar. 2001.

[32] E. Muljadi and J. T. Bialasiewicz, "Hybrid power system with a controlled energy storage," in *Proc*. 2003 *IEEE 29th IECON*, pp. 1296-1301, Vol. 2.

[33] F. Valenciaga, P. F. Puleston, and P. E. Battaiotto, "Power control of a solar/wind generation system without wind measurement: a passivity/sliding mode approach," *IEEE Trans. Energy Convers.,* vol. 18, no. 4, pp. 501-507, Dec. 2003.

[34] F. Valenciaga and P. F. Puleston, "Supervisor control for a stand-alone hybrid generation system using wind and photovoltaic energy," *IEEE Trans. Energy Convers.,* vol. 20, no. 2, pp. 398-405, Jun. 2005.

[35] S.-K. Kim, E.-S. Kim, and J.-B. Ahn, "Modeling and Control of a Grid-connected Wind/PV Hybrid Generation System," in *Proc*. 2006 *IEEE PES Transmission and Distribution Conf. Exhi.*, pp. 1202-1207.

[36] S.-K. Kim, J.-H. Jeon, C.-H. Cho, J.-B. Ahn, and S.-H. Kwon, "Dynamic Modeling and Control of a Grid-Connected Hybrid Generation System With Versatile Power Transfer," *IEEE Trans. Ind. Electron.,* vol. 55, no. 4, pp. 1677-1688, Apr. 2008.

[37] L. Chunhua, K. T. Chau, and Z. Xiaodong, "An Efficient Wind-Photovoltaic Hybrid Generation System Using Doubly Excited Permanent-Magnet Brushless Machine," *IEEE Trans. Ind. Electron.,* vol. 57, no. 3, pp. 831-839, Mar. 2010.

[38] S. Bae and A. Kwasinski, "Maximum power point tracker for a multiple-input Ćuk dc-dc converter," in *Proc*. 2009 *IEEE 31st INTELEC*, pp. 1-5.

[39] N. D. Benavides and P. L. Chapman, "Power budgeting of a multiple-input buck-boost converter," *IEEE Trans. Power Electron.,* vol. 20, no. 6, pp. 1303-1309, Nov. 2005.

[40] B. G. Dobbs and P. L. Chapman, "A multiple-input DC-DC converter topology," *IEEE Power Electron. Lett.,* vol. 1, no. 1, pp. 6-9, Mar. 2003.

[41] A. Khaligh, "A multiple-input dc-dc positive buck-boost converter topology," in *Proc*. 2008 *IEEE 23rd APEC*, pp. 1522-1526.

[42] A. Khaligh, C. Jian, and L. Young-Joo, "A Multiple-Input DC-DC Converter Topology," *IEEE Trans. Power Electron.,* vol. 24, no. 3, pp. 862-868, Mar. 2009.

[43] A. Kwasinski, "Identification of Feasible Topologies for Multiple-Input DC-DC Converters," *IEEE Trans. Power Electron.,* vol. 24, no. 3, pp. 856-861, Mar. 2009.

[44] H. Matsuo, K. Kobayashi, Y. Sekine, M. Asano, and W. Lin, "Novel solar cell power supply system using the multiple-input DC-DC converter," in *Proc*. 1998 *IEEE 20th INTELEC*, pp. 797-802.

[45] H. Matsuo, L. Wenzhong, F. Kurokawa, T. Shigemizu, and N. Watanabe, "Characteristics of the multiple-input DC-DC converter," *IEEE Trans. Ind. Electron.,* vol. 51, no. 3, pp. 625-631, Jun. 2004.

[46] L. Solero, A. Lidozzi, and J. A. Pomilio, "Design of multiple-input power converter for hybrid vehicles," *IEEE Trans. Power Electron.,* vol. 20, no. 5, pp. 1007-1016, Sep. 2005.

[47] H. Tao, A. Kotsopoulos, J. L. Duarte, and M. A. M. Hendrix, "Family of multiport bidirectional DC-DC converters," in *Proc*. 2006 *Elect. Power App.*, pp. 451-458.

[48] Q. Wang, J. Zhang, X. Ruan, and K. Jin, "Isolated Single Primary Winding Multiple-Input Converters," *accepted for publication in a future issue of IEEE Trans. Power Electron.,* Jan. 2011.

[49] L. Yan, R. Xinbo, Y. Dongsheng, L. Fuxin, and C. K. Tse, "Synthesis of Multiple-Input DC/DC Converters," *IEEE Trans. Power Electron.,* vol. 25, no. 9, pp. 2372-2385, Sep. 2010.

[50] Q. Zhijun, O. Abdel-Rahman, and I. Batarseh, "An Integrated Four-Port DC/DC Converter for Renewable Energy Applications," *IEEE Trans. Power Electron.,* vol. 25, no. 7, pp. 1877-1887, Jul. 2010.

[51] R. Zhao and A. Kwasinski, "Multiple-input single ended primary inductor converter (SEPIC) converter for distributed generation applications," in *Proc*. 2009 *IEEE ECCE*, pp. 1847-1854.

[52] S. H. Choung and A. Kwasinski, "Multiple-input dc-dc converter topologies comparison," in *Proc*. 2008 *IEEE 34th IECON*, pp. 2359-2364.

[53] L. Pieltain Fernandez, T. Gomez San Roman, R. Cossent, C. Mateo Domingo, and P. Frias, "Assessment of the Impact of Plug-in Electric Vehicles on Distribution Networks," *IEEE Trans. Power Syst.,* vol. 26, no. 1, pp. 206-213, Feb. 2011.

[54] S. W. Hadley, "Impact of Plug-in Hybrid Vehicles on the Electric Grid," Oak Ridge National Laboratory, Oak Ridge, TN, Tech. Rep. ORNL/TM-2006/554, Oct. 2006.

[55] S. W. Hadley, "Evaluating the impact of Plug-in Hybrid Electric Vehicles on regional electricity supplies," in *Proc*. 2007 *iREP Symp.*, pp. 1-12.

[56] C. Farmer, P. Hines, J. Dowds, and S. Blumsack, "Modeling the Impact of Increasing PHEV Loads on the Distribution Infrastructure," in *Proc*. 2010 *Hawaii Int. Conf. on Syst. Sci.*, pp. 1-10.

[57] S. Meliopoulos, J. Meisel, G. Cokkinides, and T. Overbye, "Power System Level Impacts of Plug-In Hybrid Vehicles: Volume II," Power Systems Engineering Research Center, Tech. Rep. PSERC Document 09-12, Oct. 2009.

[58] C. Roe, F. Evangelos, J. Meisel, A. P. Meliopoulos, and T. Overbye, "Power System Level Impacts of PHEVs," in *Proc*. 2009 *Hawaii Int. Conf. on Syst. Sci.*, pp. 1-10.

[59] K. Qian, C. Zhou, M. Allan, and Y. Yuan, "Modeling of Load Demand Due to EV Battery Charging in Distribution Systems," *IEEE Trans. Power Syst.,* vol. 26, no. 2, pp. 802-810, May 2011.

[60] K. Qian, C. Zhou, M. Allan, and Y. Yuan, "Load model for prediction of electric vehicle charging demand," in *Proc*. 2010 *Int. Conf. Power Syst. Tech.*, pp. 1-6.

[61] A. Karnama and V. Knazkins, "Scenario-based investigation of the effects of Plug-in Hybrid Electric Vehicles (PHEVs) in 11 kV substations in Stockholm," in *Proc*. 2010 *7th Int. Conf. European Energy Market*, pp. 1-6.

[62] J. A. P. Lopes, F. J. Soares, and P. M. R. Almeida, "Identifying management procedures to deal with connection of Electric Vehicles in the grid," in *Proc*. 2009 *IEEE Power Tech. Conf.*, pp. 1-8.

[63] J.-R. Won, Y.-B. Yoon, and K.-J. Lee, "Prediction of electricity demand due to PHEVs (Plug-In Hybrid Electric Vehicles) distribution in Korea by using diffusion model," in *Proc*. 2009 *IEEE Asia and Pacific Transmission & Distribution Conf.*, pp. 1-4.

[64] D. Mercer, "Scenarios made easy," *Long Range Planning,* vol. 28, no. 4, pp. 7-8, Aug. 1995.

[65] F. M. Bass, "A new product growth model for consumer durables," *Manage. Sci.,* vol. 15, no. 5, pp. 215-227, Jan. 1969.

[66] P. Papadopoulos, S. Skarvelis-Kazakos, I. Grau, L. M. Cipcigan, and N. Jenkins, "Predicting Electric Vehicle impacts on residential distribution networks with Distributed Generation," in *Proc*. 2010 *IEEE Vehicle Power and Propulsion Conf.*, pp. 1-5.

[67] J. Taylor, A. Maitra, M. Alexander, D. Brooks, and M. Duvall, "Evaluation of the impact of plug-in electric vehicle loading on distribution system operations," in *Proc*. 2009 *IEEE PES Gen. Meet.*, pp. 1-6.

[68] S. Huang and D. Infield, "The impact of domestic Plug-in Hybrid Electric Vehicles on power distribution system loads," in *Proc*. 2010 *Int. Conf. Power Syst. Tech.*, pp. 1-7.

[69] R. Garcia-Valle and J. G. Vlachogiannis, "Letter to the Editor: Electric Vehicle Demand Model for Load Flow Studies," *Elect. Power Compo. Syst.,* vol. 37, no. 5, pp. 577-582, May 2009.

[70] *The United Kingdom 2000 Time Use Survey Technical Report 2003*. Available:http://www.statistics.gov.uk/downloads/theme_social/UKTUS_TechReport.pdf

[71] J. Axsen and K. S. Kurani, "Anticipating plug-in hybrid vehicle energy impacts in California: Constructing consumer-informed recharge profiles," *Transp. Res.: Part D: Transport Environ.,* vol. 15, no. 4, pp. 212-219, Jun. 2010.

[72] L. Kelly, "Probabilistic Modelling of Plug-in Hybrid Electric Vehicle Impacts on Distribution Networks in British Columbia," M.S. thesis, Dept. Mech. Eng., Univ. Victoria, Victoria, Canada, 2009.

[73] J. W. May, "Plugging In: A Feasibility Study on Public Plug-In Vehicle Charging Infrastructure Investment," M.S. thesis, Sch. Environ., Duke Univ., Durham, U.S., 2009.

[74] S. Li, T. A. Haskew, and L. Xu, "Conventional and novel control designs for direct driven PMSG wind turbines," *Elect. Power Syst. Research,* vol. 80, no. 3, pp. 328-338, Mar. 2010.

[75] K. K. Leung, W. A. Massey, and W. Whitt, "Traffic models for wireless communication networks," in *Proc*. 1994 *IEEE INFOCOM '94*, pp. 1029-1037.

[76] K. K. Leung, W. A. Massey, and W. Whitt, "Traffic models for wireless communication networks," *IEEE J. Sel. Areas Commun.,* vol. 12, no. 8, pp. 1353-1364, Oct. 1994.

[77] W. A. Massey and W. Whitt, "A Stochastic Model to Capture Space and time Dynamics in Wireless Communication Systems," *Probability in the Eng. & Info. Sci.,* vol. 8, no. 4, pp. 541-569, Oct. 1994.

[78] V. G. Kulkarni, *Modeling, Analysis, Design, and Control of Stochastic Systems*, 1st ed.: Springer, 1999.

[79] S. Braithwait, "Behavior Modification," *IEEE Power Energy Mag.,* vol. 8, no. 3, pp. 36-45, May-Jun. 2010.

[80] A. Brooks, E. Lu, D. Reicher, C. Spirakis, and B. Weihl, "Demand Dispatch," *IEEE Power Energy Mag.,* vol. 8, no. 3, pp. 20-29, May-Jun. 2010.

[81] J. Medina, N. Muller, and I. Roytelman, "Demand Response and Distribution Grid Operations: Opportunities and Challenges," *IEEE Trans. Smart Grid,* vol. 1, no. 2, pp. 193-198, Sept. 2010.

[82] M. Parvania and M. Fotuhi-Firuzabad, "Demand Response Scheduling by Stochastic SCUC," *IEEE Trans. Smart Grid,* vol. 1, no. 1, pp. 89-98, Jun. 2010.

[83] F. Rahimi and A. Ipakchi, "Demand Response as a Market Resource Under the Smart Grid Paradigm," *IEEE Trans. Smart Grid,* vol. 1, no. 1, pp. 82-88, Jun. 2010.

[84] J. Gonder, T. Markel, M. Thornton, and A. Simpson, "Using Global Positioning System Travel Data to Assess Real-World Energy Use of Plug-In Hybrid Electric Vehicles," *Transp. Research Rec.: J. Transp. Research Board,* vol. 2017, no. 1, pp. 26-32, Dec. 2007.

[85] J. Gonder, T. Markel, M. Thornton, and A. Simpson, "Using GPS Travel Data to Assess the Real World Driving Energy Use of Plug-In Hybrid Electric Vehicles (PHEVs)," in *Proc*. 2007 *Annu. Meet. Transp. Research Board*, pp. 1-11.

[86] P. Chavan, K. Tufte, C. M. Monsere, M. Stephens, and R. L. Bertini, "Extending the Use of Archived ITS Data As a Potential Management Tool to Evaluate Traveler Information on Dynamic Message Signs," in *Proc*. 2008 *Annu. Meet. Transp. Research Board*, pp. 1-10.

[87] M. Dalgleish and N. Hoose, *Highway traffic monitoring and data quality*, 1st ed.: Artech House Publishers, 2008.

[88] A. Kwasinski, "Analysis of electric power architectures to improve availability and efficiency of air conditioning systems," in *Proc*. 2008 *IEEE 30th INTELEC*, pp. 1-8.

[89] A. Kwasinski, "Evaluation of dc Voltage Levels for Integrated Information Technology and Telecom Power Architectures," in *Proc*. 2009 *4th TELESCON - Power Supply Quality and Efficiency*, pp. 1-7.

[90] P. M. Anderson and A. Bose, "Stability Simulation Of Wind Turbine Systems," *IEEE Trans. Power App. Syst.,* vol. PAS-102, no. 12, pp. 3791-3795, Dec. 1983.

[91] A. Murdoch, J. R. Winkelman, S. H. Javid, and R. S. Barton, "Control Design and Performance Analysis of a 6 MW Wind Turbine-Generator," *IEEE Trans. Power App. Syst.,* vol. PAS-102, no. 5, pp. 1340-1347, May 1983.

[92] M. G. Villalva, J. R. Gazoli, and E. R. Filho, "Comprehensive Approach to Modeling and Simulation of Photovoltaic Arrays," *IEEE Trans. Power Electron.,* vol. 24, no. 5, pp. 1198-1208, May 2009.

[93] S. Cuk and R. D. Middlebrook, "Advances in Switched-Mode Power Conversion Part I," *IEEE Trans. Ind. Electron.,* vol. IE-30, no. 1, pp. 10-19, Feb. 1983.

[94] M. E. Haque, K. M. Muttaqi, and M. Negnevitsky, "Control of a stand alone variable speed wind turbine with a permanent magnet synchronous generator," in *Proc*. 2008 *IEEE PES Gen. Meet.*, pp. 1-9.

[95] M. E. Haque, M. Negnevitsky, and K. M. Muttaqi, "A Novel Control Strategy for a Variable-Speed Wind Turbine With a Permanent-Magnet Synchronous Generator," *IEEE Trans. Ind. App.,* vol. 46, no. 1, pp. 331-339, Jan.-feb. 2010.

[96] D. Aliprantis, S. Papathanassiou, M. Papadopoulos, and A. Kladas, "Modeling and Control of a Variable-speed Wind Turbine Equipped with Permanent Magnet Synchronous Generator," in *Proc*. 2000 *Int. Conf. Elect. Mach.*, pp. 558-562.

[97] M. N. Eskander, "Neural network controller for a permanent magnet generator applied in a wind energy conversion system," *Renewable Energy,* vol. 26, no. 3, pp. 463-477, Jul. 2002.

[98] N. Mohan, T. Underland, and W. Robbins, *Power Electronics; Converters, Applications, and Design*, 3rd ed. Hoboken, NJ: John Wiley and Sons, 2003.

[99] O. Wasynezuk, "Dynamic Behavior of a Class of Photovoltaic Power Systems," *IEEE Trans. Power App. Syst.,* vol. PAS-102, no. 9, pp. 3031-3037, Sept. 1983.

[100] A. F. Boehringer, "Self-Adapting dc Converter for Solar Spacecraft Power Supply Selbstanpassender Gleichstromwandler fÃ¼r die Energieversorgung eines Sonnensatelliten," *IEEE Trans. Aero. Electron. Syst.,* vol. AES-4, no. 1, pp. 102-111, Jan. 1968.

[101] K. H. Hussein, I. Muta, T. Hoshino, and M. Osakada, "Maximum photovoltaic power tracking: an algorithm for rapidly changing atmospheric conditions," *Proc. Inst. Electr. Eng.−Generation, Transmission, Distrib.,* vol. 142, no. 1, pp. 59-64, Jan. 1995.

[102] W. Wenkai, N. Pongratananukul, Q. Weihong, K. Rustom, T. Kasparis, and I. Batarseh, "DSP-based multiple peak power tracking for expandable power system," in *Proc*. 2003 *IEEE 18th APEC*, pp. 525-530.

[103] R. Haberman, *Mathematical Models: Mechanical Vibrations, Population Dynamics, and Traffic flow*, SIAM ed. Philadelphia, PA: Society for Industrial Mathematics 1998.

[104] J. Spurk and N. Aksel, *Fluid Mechanics*, 2nd ed.: Springer, 2008.

Vita

Sung Woo Bae received the Bachelor of Science degree in electrical and computer engineering from *Hanyang* University, Seoul, Korea in February 2006. He graduated summa cum laude from *Hanyang* University. He was the recipient of the Grand Prize for his excellent design at the National Electrical Engineering Design Contest in 2005, presented by the Minister of Commerce, Industry and Energy of the Republic of Korea. In May 2009, Mr. Bae earned the Master of Science in Engineering degree in electrical and computer engineering from the University of Texas at Austin. During his doctoral studies, his main research interests are focused on renewable energy, microgrid, plug-in electric vehicles, and smart grid power systems.

Email: sungwbae@utexas.edu

This dissertation was typed by the author.